ACADÉMIE
DES SCIENCES
INSTITUT DE FRANCE

Comptes Rendus
Mécanique

Pierre Latil, Malo Valmalle, Benjamin Smaniotto, Clément Jailin and François Hild

Mechanics-guided data-enhanced kinematic models for time-resolved DVC

Volume 354 (2026), p. 495-525

Online since: 2 June 2026

https://doi.org/10.5802/crmeca.370

The Comptes Rendus. Mécanique *are a member of the Mersenne Center for open scientific publishing*
www.centre-mersenne.org — e-ISSN : 1873-7234

ACADÉMIE DES SCIENCES
INSTITUT DE FRANCE

Comptes Rendus. Mécanique
2026, Vol. 354, p. 495-525
https://doi.org/10.5802/crmeca.370

Research article

Mechanics-guided data-enhanced kinematic models for time-resolved DVC

Pierre Latil [a], Malo Valmalle [a], Benjamin Smaniotto [a], Clément Jailin [a] and François Hild [*, a]

[a] Université Paris-Saclay, CentraleSupélec, ENS Paris-Saclay, CNRS, LMPS–Laboratoire de Mécanique Paris-Saclay, 91190 Gif-sur-Yvette, France

E-mail: francois.hild@ens-paris-saclay.fr

Abstract. X-ray Computed Tomography (XCT) combined with Digital Volume Correlation (DVC) enables for internal displacement and strain measurements in deforming materials. The long acquisition time of tomographic scans restricts analyses to a few static loading steps and prevents from time-dependent or nonlinear mechanism quantification. Projection-based DVC (P-DVC) addresses this limitation by exploiting projections acquired during continuous loading, providing substantially higher temporal sampling.

This study assesses a spacetime framework of projection-enhanced DVC for the *in situ* investigation of a 3D-printed lattice. Global DVC displacement fields are used to construct reduced spatial bases, namely, (i) a pure data-driven basis, (ii) a mechanics-only basis derived from an elastic compression solution, and (iii) a hybrid mechanics-data basis combining both. P-DVC then exploits the projections to identify the temporal amplitudes associated with these modes, thereby reconstructing the time-resolved kinematics with a resolution of 3.7 s, nearly two orders of magnitude faster than conventional 3D-to-3D DVC.

Nonlinear mechanisms were detected ahead of their clear expression in tomographic reconstructions. The hybrid reduced-order approach provided interpretable kinematic fields while preserving the predictive accuracy of data-driven strategies. The projection-enhanced DVC framework thus enabled for temporally dense and spatially resolved *in situ* measurements, providing the type of rich datasets required for the identification and learning of complex constitutive models.

Keywords. *In situ* tests, Digital Volume Correlation (DVC), projection-based DVC (P-DVC), spacetime analyses, model reduction.

Funding. This work has been supported by the French "Agence Nationale de la Recherche" through the "ADAM" project (Accelerated Design of Architectured Materials, ANR-22-PEXD-0002) and the "Investissements d'avenir" program (ANR-10-EQPX-37, MATMECA grant).

Manuscript received 3 December 2025, revised 1 April 2026, accepted 18 May 2026, online since 2 June 2026.

1. Introduction

X-ray Computed Tomography (XCT) has become a widely used imaging technique in experimental mechanics as it enables for the non-destructive reconstruction of three-dimensional microstructures from series of X-ray radiographs [1]. When combined with Digital Volume Correlation (DVC), XCT provides access to full-field displacement and strain measurements within the bulk of materials [2–4]. This capability has considerably advanced the study of heterogeneous

* Corresponding author

materials and architected structures, allowing for the quantitative characterization of deformation mechanisms and the correlation of the local kinematics with evolving microstructural features. With the development of dedicated *in situ* loading devices compatible with X-ray scanners [5,6], it has become possible to probe mechanical responses under complex loading conditions.

Despite these advances, standard DVC procedures suffer from a fundamental limitation, namely, each tomographic volume requires hundreds to thousands of projections to be collected while the specimen is maintained static. Depending on the imaging system, a single scan may last from several minutes to several hours [7]. Consequently, DVC analyses are restricted to a limited number of discrete and static loading steps. The material response between two consecutive scans is not accessible, and time-dependent phenomena such as viscosity or crack propagation cannot be adequately captured. Moreover, motions during long scans may introduce artifacts that deteriorate the reconstruction quality [8]. To mitigate this effect, acquisitions are typically started only after the measured force stabilizes [9].

Two main strategies have been explored to alleviate these limitations. One approach, on the hardware side, consists in performing very fast scans at synchrotron facilities using high-brilliance X-ray beams and high-speed detectors [8,10]. Although this route allows for 20 to 1000 Hz temporal resolutions (i.e. volume acquisitions per second), it comes with drawbacks such as limited accessibility, limited field of view, high radiation doses, and reconstruction artifacts caused by vibrations and motion blur. In addition to improving the image acquisition (or optimizing current systems [11]), an alternative route, on the software side, relies on projection-based methods that exploit the temporal richness of radiographs without reconstructing full volumes. Projection-based Digital Volume Correlation (P-DVC) belongs to this class. These methods make use of a reference reconstructed volume and a series of 2D X-ray radiographs recorded during continuous loading. By correlating these projections with the 3D reference image, P-DVC enables for the measurement of internal kinematic fields at intermediate loading states, effectively extending DVC into the temporal dimensions by several orders of magnitude [4,12]. In this way, P-DVC enables for four-dimensional (3D in space + 1D in time) kinematic measurements over complete loading histories with significantly shorter acquisition times and lower radiation doses.

Recent studies have highlighted the potential of P-DVC for capturing the full spatiotemporal evolution of deformations of complex materials. Different formulations have been proposed, either based on spacetime discretizations of the displacement fields [12], or on spacetime approaches in which spatial modes are obtained from scan-wise DVC and only the temporal amplitudes are identified from radiographs [13,14]. These strategies have been successfully applied to fiber-reinforced polymers [15], polymer composites [14], and mechanical metamaterials [13,16,17], showing that a limited number of spatial modes was sufficient to reconstruct the kinematic history up to specimen failure.

In parallel, architected materials fabricated by Additive Manufacturing (AM) have attracted growing interest for their ability to decouple geometry and material properties [18]. Lattice structures in particular may exhibit highly tunable deformation behaviors such as bending, buckling, and controlled collapse [19]. However, their mechanical performance is strongly affected by process-induced features, including surface roughness, porosity, and residual stresses induced by Selective Laser Melting (SLM) [20]. These imperfections introduce variability and may trigger premature failure [16,17], underscoring the importance of detailed *in situ* investigations. While DVC is well suited for such analyses, the limited temporal resolution of classical approaches restricts its ability to capture fast or nonlinear events such as damage initiation and growth [4,14].

The present study addresses this challenge by projection-augmenting DVC to investigate the mechanical response of an SLM-fabricated body-centered cubic (BCC) lattice made from

AlSi10Mg powder. Full 3D volumes acquired at selected loading steps are analyzed with finite-element based DVC to measure high-resolution displacement and strain fields. In parallel, time-resolved radiographs acquired throughout the loading history are exploited via P-DVC to interpolate the deformation states between scans. This spacetime approach yields temporally dense and spatially resolved measurements, enabling for the identification of deformation mechanisms as they develop.

The objective of this work is to demonstrate, on a BCC lattice subjected to uniaxial compression, that a projection enhanced DVC framework recovers the time-resolved (4D) internal kinematics for each treated projection while preserving the spatial fidelity of scan-wise FE-DVC. Three reduced kinematic descriptions are benchmarked, namely, (i) a data-driven SVD basis, (ii) a mechanics-only elastic basis, and (iii) a hybrid basis that complements elasticity with SVD modes of the residual motions. The performance is assessed against DVC results in terms of amplitude monitoring, displacement error, projection residuals, computational cost, and sensitivity to the onset of shear banding and damage. To the best of the authors' knowledge, this is the first study to unify DVC and P-DVC with side-by-side, mechanically-enhanced mode-truncated kinematic models. This combination enables not only for early monitoring deviation from elasticity between each projection, but also provides physically interpretable, yet data-rich, kinematic models that open new possibilities for the identification of advanced constitutive models.

2. Material and methods

This section presents the studied lattice and the *in situ* XCT compression test that was carried out. Last, the DVC and P-DVC protocols are described.

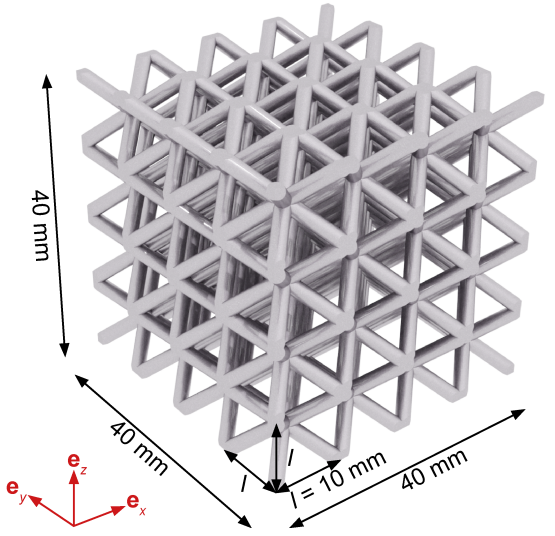

Figure 1. CAD model of the studied BCC lattice.

2.1. *Studied sample*

The sample considered herein is a Body Centered Cubic (BCC) lattice of outer dimension $40 \times 40 \times 40\,\mathrm{mm}^3$ (Figure 1). The unit cell, of outer dimension $l \times l \times l = 10 \times 10 \times 10\,\mathrm{mm}^3$, contains 8 beams

of circular cross section of diameter 2 mm and of length $l_b = (l/2)\sqrt{3} \approx 8.66$ mm that connect the center of the unit cell to its corners. These nominal values were used to design the lattice in the CAD software. The resulting CAD file was then used to produce the sample by Selective Laser Melting (SLM) using an EOS M290 LPBF (EOS GmbH) machine with AlSi10Mg powder. The printing parameters and material composition are reported in Appendix A.

2.2. In situ *compression test*

The compressed sample was imaged using X-ray computed microtomography (CT) [1]. Such imaging technique is non-intrusive and provides 3D images of samples tested *in situ* [21]. The test was carried out under displacement-control and the force was measured by the load cell of the testing machine (Figure 2(a)–(b)). Compression platens, made of commercial aluminum alloy, were used (Figure 2(b)) to transmit the load from the *in situ* testing machine to the sample. Unlike many other *in situ* testing machines [21], the one used herein does not entirely rotate, only the inner platens are rotating. No specific surface preparation was performed prior to the compression test. The sample was loaded up to failure (Figure 2(e)), with scans taken at 0.25 mm stroke intervals, the load velocity being 5 µm/s. The hardware parameters of the *in situ* setup are gathered in Appendix B. Series of 1000 radiographs over 360° revolutions were acquired in a little more than 10 min to reconstruct 3D images from the CT scans using the Simultaneous Iterative Reconstruction Technique (SIRT) [22] after flat field [23] and beam hardening corrections. The reconstructed volumes covered $98.0 \times 98.0 \times 77.4\,\text{mm}^3$ with a voxel size of 100.8 µm ($972 \times 972 \times 768$ voxels).

The *in situ* test consisted of sequences with a loading part (when the crosshead was moved but with no rotation of the turntable), followed by dwell (i.e. no motion of the crosshead and the turntable), and then by a tomographic scan (no motion of the crosshead and full rotation of the turntable). During each step, which includes loading and dwell, radiographs were acquired on the fly. Two temporal bases are considered. First, the time t since the start of the experiment. Second, the time duration for scanning, which corresponds to turns T. The turns are gray shaded in the figures where temporal histories are reported (Figure 2(c)). Figure 2(a) shows the force F vs. prescribed displacement U after a preload of about 1 kN was applied to maintain the sample during the reference scan acquisitions corresponding to turns 0 and 00, not shown here). This curve exhibits a linear regime until turn $T = 2$, i.e. $U \approx 0.75$ mm, then a nonlinear regime between turns $T = 3$ and 7, and finally a small softening regime between turns $T = 7$ and 9 until failure (between turns $T = 9$ and 10 (Figure 2(a) and (e)). Load drops are visible at each interruption (Figure 2(a)); they reflect relaxations that occurred when the loading was stopped before scan acquisitions. The non monotonic decrease of force during scan acquisitions (see inset of Figure 2(a)) was due to minute misalignment of the compression platens with respect to the rotation axis. Twelve tomographic scans were acquired, namely, two in the reference configuration for uncertainty quantification (i.e. $T = 0$ and 00), nine in deformed configurations ($T = 1-9$) and one after failure of the specimen ($T = 10$).

Figure 2(c) shows the testing machine crosshead displacement U history since the start of step 1. If the loading time is 50 s at each step (i.e. 0.25 mm at 5 µm/s), the total duration of each step is variable, between 2 and 12 min, because it includes some time to setup the projection acquisition and launch the testing machine crosshead displacement, the dwell — manually interrupted when the force seemed to be stable — and some time to get back in scan acquisition mode. The experiment lasted 2 h and 49 min. Besides the CT scans, a total of $\mathcal{N} = 9362$ projections was acquired during the nine steps at a constant projection angle $\theta(t) = 0$ (i.e. in the $y-z$ plane, Figure 2(b)).

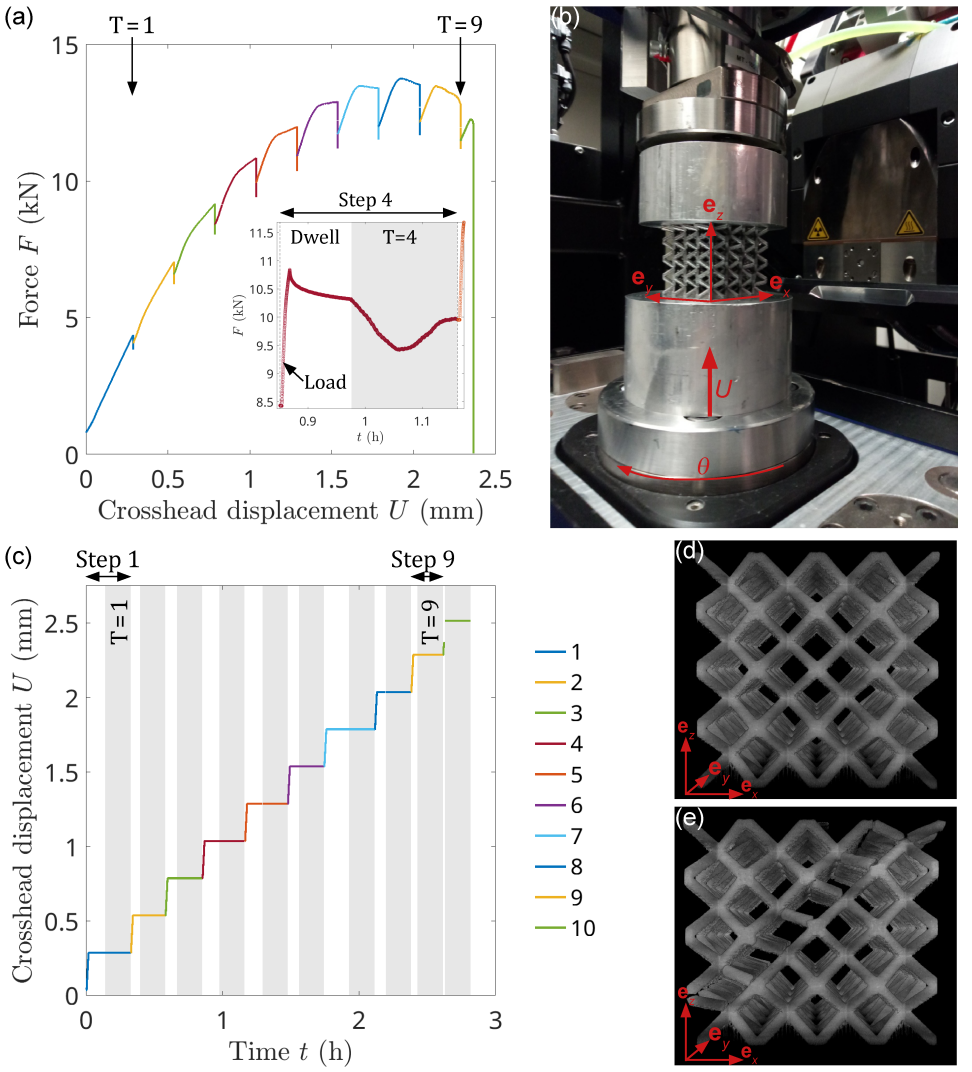

Figure 2. (a) Force F vs. crosshead displacement U. Inset: force F vs. time t for step 4 composed of loading with $\theta(t) = 0$, dwell where $\dot{U} = 0$ and $\theta(t) = 0$, and (gray shaded) scan acquisition T with $0 \leq \theta(t) \leq 2\pi$. (b) Picture of the sample during the *in situ* test at $\theta = 0$. (c) Crosshead displacement U vs. time t (the gray shaded areas highlight the scanning turns). (d)–(e) 3D renderings of the sample for $U = 1$ mm stroke ($T = 4$) and at failure ($T = 10$), respectively.

Projection enhanced DVC [13] generally consists of first performing DVC analyses on the 3D reconstructed volumes. The corresponding time frame is thus parameterized by the turn number T. From these DVC fields, a singular value decomposition is performed to extract the dominant spatial components [16]. The corresponding temporal components are then obtained via P-DVC, which registers each individual radiograph, whose time frame is defined by t. In the present study, different spatial bases are constructed and P-DVC is run to measure the associated temporal amplitudes. If a quantity depends on t, it is related to P-DVC, and if it is a function of T, it generally corresponds to DVC analyses.

2.3. *DVC stage*

In DVC, the conservation of gray levels of image I is assumed throughout the experiment. This hypothesis states that the gray level (absorption) of each material point $\mathbf{x}$ is considered constant between different 3D reconstructions. Hence, for each deformed image $I_T(\mathbf{x}) = I(\mathbf{x}, T)$, there is a displacement field $\mathbf{u}(\mathbf{x}, T)$ such that

$$I_T(\mathbf{x}) = I_0\big(\mathbf{x} - \mathbf{u}(\mathbf{x}, T)\big), \quad \forall\ T \in [0, T_{\text{end}}], \tag{1}$$

where I_0 is the 3D image of the reference state (i.e. when the displacement $\mathbf{u}(\mathbf{x}, T = 0) = \mathbf{0}$). Note that, contrary to standard DVC procedures written in Lagrangian setting, this equation is written in the Eulerian framework. This formulation eases the transition toward P-DVC and only requires a straightforward change of frame in the implementation. The measured displacement field $\mathbf{u}_{\text{meas}}$ is determined by minimizing the sum of squared gray level differences

$$\Phi^2_{\text{DVC}}\big(\{\boldsymbol{v}\}\big) = \sum_{\text{ROI}} \big(I_0\big(\mathbf{x} - \mathbf{u}\big(\mathbf{x}, \{\boldsymbol{v}\}\big)\big) - I_T(\mathbf{x})\big)^2, \tag{2}$$

where $\{\boldsymbol{v}\}$ denotes the column vector that gathers all nodal displacements, ROI the selected region of interest, and the gray level residual $\rho_{\text{DVC}}(\mathbf{x}, T)$ at each voxel $\mathbf{x}$ reads

$$\rho_{\text{DVC}}(\mathbf{x}, T) = I_0\big(\mathbf{x} - \mathbf{u}\big(\mathbf{x}, \{\boldsymbol{v}\}\big)\big) - I_T(\mathbf{x}). \tag{3}$$

Note that this DVC residual is the only quantity that will be displayed in the reference coordinate system $\widehat{\mathbf{x}}$ (with $\mathbf{u}(\mathbf{x}, t) \coloneqq \mathbf{x} - \widehat{\mathbf{x}} = \widehat{\mathbf{u}}(\widehat{\mathbf{x}}, t)$).

The DVC solution is penalized by mechanical regularization expressed with the equilibrium gap

$$\phi^2_m\big(\{\boldsymbol{v}\}\big) = \{\boldsymbol{v}\}^\top [\mathbf{K}]^\top [\mathbf{K}] \{\boldsymbol{v}\}, \tag{4}$$

such that

$$\big\{\boldsymbol{v}(T)\big\}_{\text{meas}} = \arg\min_{\{\boldsymbol{v}\}} \big(\Phi^2_{\text{DVC}}\big(\{\boldsymbol{v}\}\big) + w_m \Phi^2_m\big(\{\partial\boldsymbol{v}\}\big)\big), \tag{5}$$

where $\{\partial\boldsymbol{v}\}$ denotes the column vector of incremental nodal displacements, and $[\mathbf{K}]$ the rectangular stiffness matrix associated with bulk and free surface nodes. The relative contribution of both terms is controlled by the weighting of the mechanical regularization term. This weight, w_m, is proportional to the regularization length ℓ_m raised to the power 4 [24].

2.3.1. *Mesh of the reference configuration*

In the present case, unstructured meshes made of 4-noded tetrahedra (T4) are chosen to allow for a faithful description of external surfaces [25]. This T4 mesh was obtained directly from the surfacic STL file of the sample (Figure 1) using Matlab PDE toolbox. Therefrom, the nodal coordinates were scaled with respect to the CT resolution (i.e. 100.8 µm/vx, Figure 3(a)). It resulted in $\mathcal{N}_{\text{node}} = 30\,155$ and $\mathcal{N}_{\text{elem}} = 97\,893$ (Figure 3(a)) with an average element length of ≈ 4.6 vx (≈ 0.5 mm), which allows for a rather good description of the beams within the sample (Figure 3(b)). The mesh size was chosen as a compromise between an accurate description of the lattice surfaces and computational cost. In the present case, the average element length remained much smaller than the selected regularization length, so that the measured kinematics was mainly controlled by the mechanical regularization rather than by individual nodal fluctuations.

To take into account (i) the possible 3D printing uncertainty, (ii) the small preload in the reference configuration $T = 0$ and $T = 00$, and (iii) the image (voxel) coordinates, backtracking was performed using DVC so that the mesh was perfectly superimposed onto the image I_{00} [26], see Figure 4.

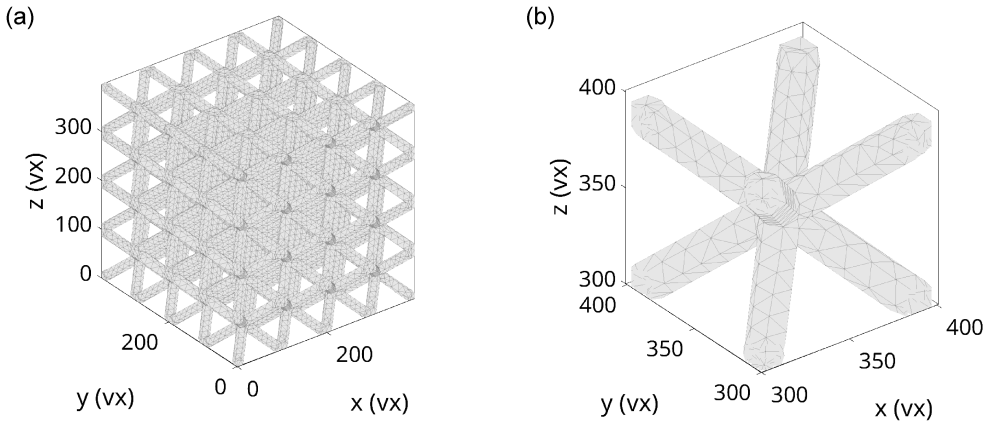

Figure 3. (a) T4 mesh of the sample at CT voxel scale. (b) Closeup view of a lattice knot.

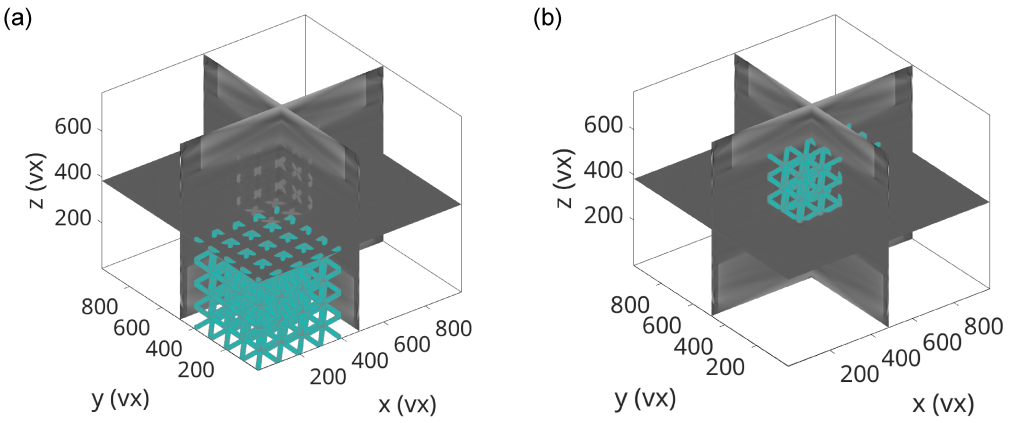

Figure 4. (a) Mesh initial position after scaling to CT image coordinates. (b) Mesh position after backtracking.

2.3.2. *Uncertainty quantification*

The reconstructed volumes were registered using the Correli 3.2 framework [27] in which Hencky regularization [28] was implemented (Appendix B). The DVC uncertainties were evaluated for five regularization lengths $\ell_m \in \{50, 125, 250, 500, 1000\}$ vx with the backtracked mesh (Figure 3) as a reference. Noise floors were assessed from the two reference scans ($T = 0$ and $T = 00$). After removing the rigid-body motions, the standard deviations of nodal displacement components were computed (Figure 5).

The measurement uncertainties were very close for the three spatial directions for a given regularization length. The (classical) trade-off between measurement uncertainty and regularization length was found, namely, the lower the regularization length, the higher the standard displacement uncertainty [29]. It is observed that the uncertainty level was not solely controlled by acquisition noise since the power $-3/2$ dependence of the displacement uncertainty was not followed [29]. This result proves that other sources of error also occurred, which was expected when dealing with tomographic acquisitions [4]. These additional sources of error are likely related to reconstruction artifacts. In the present case, they were mitigated by a fine calibration of

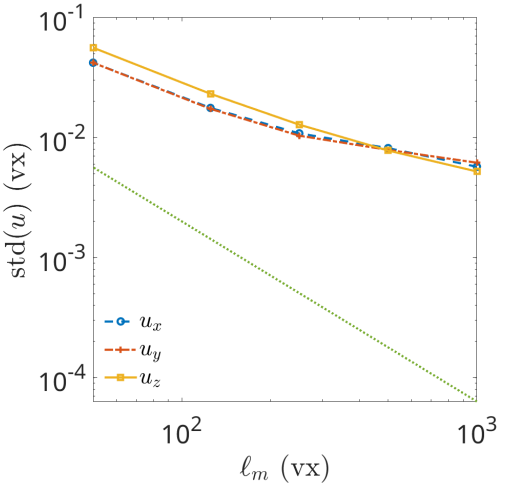

Figure 5. Standard displacement uncertainty vs. regularization length ℓ_m for all three displacement components. The green dashed line shows the power −3/2 trend expected when the uncertainty is solely controlled by white and Gaussian acquisition noise.

the projection geometry (inspired from Ref. [30]), beam hardening correction, and flat-field corrections based on multiple gain maps [23]. For regularization lengths greater than 50 vx, standard displacement uncertainties as low as $\gamma_u = 3 \times 10^{-2}$ vx were reached thanks to the regularization strategy used herein.

2.3.3. *Direct DVC calculations*

The DVC analyses were run for the 9 deformed scans using the backtracked mesh (Figure 3) and the measured displacement field of the previous scan $\mathbf{u}(\mathbf{x}, T-1)$ as initial guess. Although the displacement field from the previous scan was used as an initial guess, each deformed scan was registered with respect to the reference scan I_0, so that the adopted DVC formulation was total. The DVC calculations were stopped when the L2-norm of displacement corrections was less than 10^{-2} vx (Table 8). This criterion was chosen so that the final iterative corrections remain less than the measurement uncertainty and negligible with respect to the measured displacement amplitudes. Table 8 lists the main parameters of the FE-DVC procedure. Figure 6(a) shows the change of the dimensionless root mean square (RMS) gray level residual $\Phi^{\star}_{\mathrm{DVC}} = \Phi_{\mathrm{DVC}}/\Delta I_0$, where $\Delta I_0 = \max\big(I_0(\cdot)\big) - \min\big(I_0(\cdot)\big)$ denotes the dynamic range of the reference scan (including air and the sample but not the compression platens), as a function of the equilibrium gap Φ_m for five different regularization lengths $\ell_m \in \{50, 125, 250, 500, 1000\}$ vx. The fact that the gray level residuals remained rather close to these minimum levels when the sample was deformed is an indication that the registrations were successful. When the regularization length was increased, the equilibrium gap Φ_m decreased as more weight was put on the penalty term. Conversely, the gray level residuals increased as the sample was more deformed for large regularization lengths. This trend indicates that the regularization was too strong for the largest regularization lengths (i.e. Hencky elasticity was no longer sufficient to globally account for the underlying behavior). This observation is especially true from $T = 4$ onward. The nearly unchanged gray-level residuals up to scan $T = 4$ indicate that this regularization remained consistent with the measured data during the early loading stages, whereas the subsequent increase reveals the onset of deformation mechanisms that were no longer fully captured by the simplified mechanical assumption.

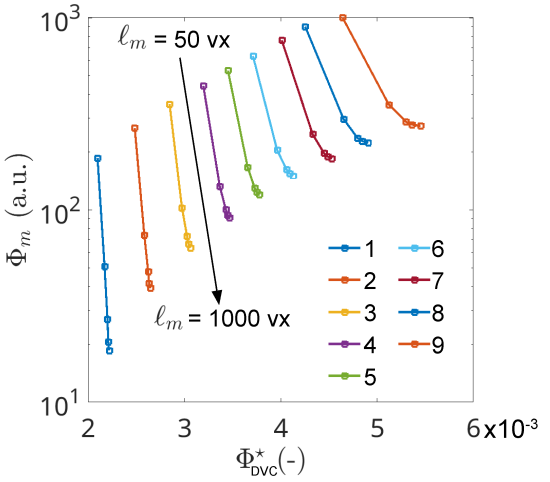

Figure 6. Mechanical residual Φ_m vs. dimensionless gray level residual $\Phi^\star_{\mathrm{DVC}}$ for the nine analyzed scans when $T \in [1,9]$ and the regularization length ℓ_m varied from 50 to 1000 vx.

One of the criteria used to select the regularization weight consists in looking for the maximum curvature (i.e. L-curve criterion [31]) in the previous plot for a given deformation step (e.g. for the maximum deformation before fracture, Figure 6). According to that criterion, the regularization length $\ell_m = 125$ vx provided the best balance between $\Phi^\star_{\mathrm{DVC}}$ and Φ_m. This result applied to all the considered deformation steps and $\ell_m = 125$ vx ($\ell_m \approx 12.6$ mm) was therefore selected.

At the current resolution, no contrast existed within the printed parts, i.e. no porosities were visible at the 100.8 µm/vx scale (Figure 7(a)). As a result DVC mainly acts on the material/air interface (Figure 7(b)). In that context, using a sufficiently fine mesh remained necessary to represent the lattice geometry accurately, while the local kinematics was mainly driven by mechanical regularization. Figure 7(b) also shows that the local maximum gray level residuals were rather small and less than 2 % of the dynamic range ΔI_0, indicating trustful results.

The measured displacement field when $T = 9$ displayed in Figure 7(c)–(e) exhibits a shape that could be attributed to a simple elastic compression with $u_z \approx 20$ vx on the lower row of the lattice, and $u_z \approx 0$ vx on the top row. Looking at the transverse displacements u_x and u_y corresponding to the boundary conditions (BC) (i.e. on the platen/sample interfaces), one distinguishes two different behaviors. The lower row of the lattice is such that $u_x = u_y = 0$, and the top row displays a significant Poisson's effect with the displacement amplitudes in the x and y direction of about ± 10 vx. This difference is due to the fact that the bottom layer has ribs between beams, as a support material for SLM printing purposes (which was not meshed) while the top row does not. Thus, the contact surfaces at the top of the sample allowed for Poisson expansion throughout the experiment.

2.4. *P-DVC stage*

Projection-based DVC uses the undeformed initial 3D image $I_0(\mathbf{x})$ of an object that is deformed with a displacement field $\mathbf{u}(\mathbf{x}, t)$. This deformed 3D image $I_0\big(\mathbf{x} - \mathbf{u}(\mathbf{x}, t)\big)$ is numerically projected using the projector $\Pi_{\theta(t)}$, which depends on the CT setup geometry parameters [32,33]. The corresponding (numerical) projection $\Pi_{\theta(t)}\big[I_0\big(\cdot - \mathbf{u}(\cdot)\big)\big](\mathbf{r})$ is compared to the real projection $p\big(\mathbf{r}, \theta(t)\big)$ (i.e. acquired with the X-ray tomograph) assuming the conservation of gray levels of

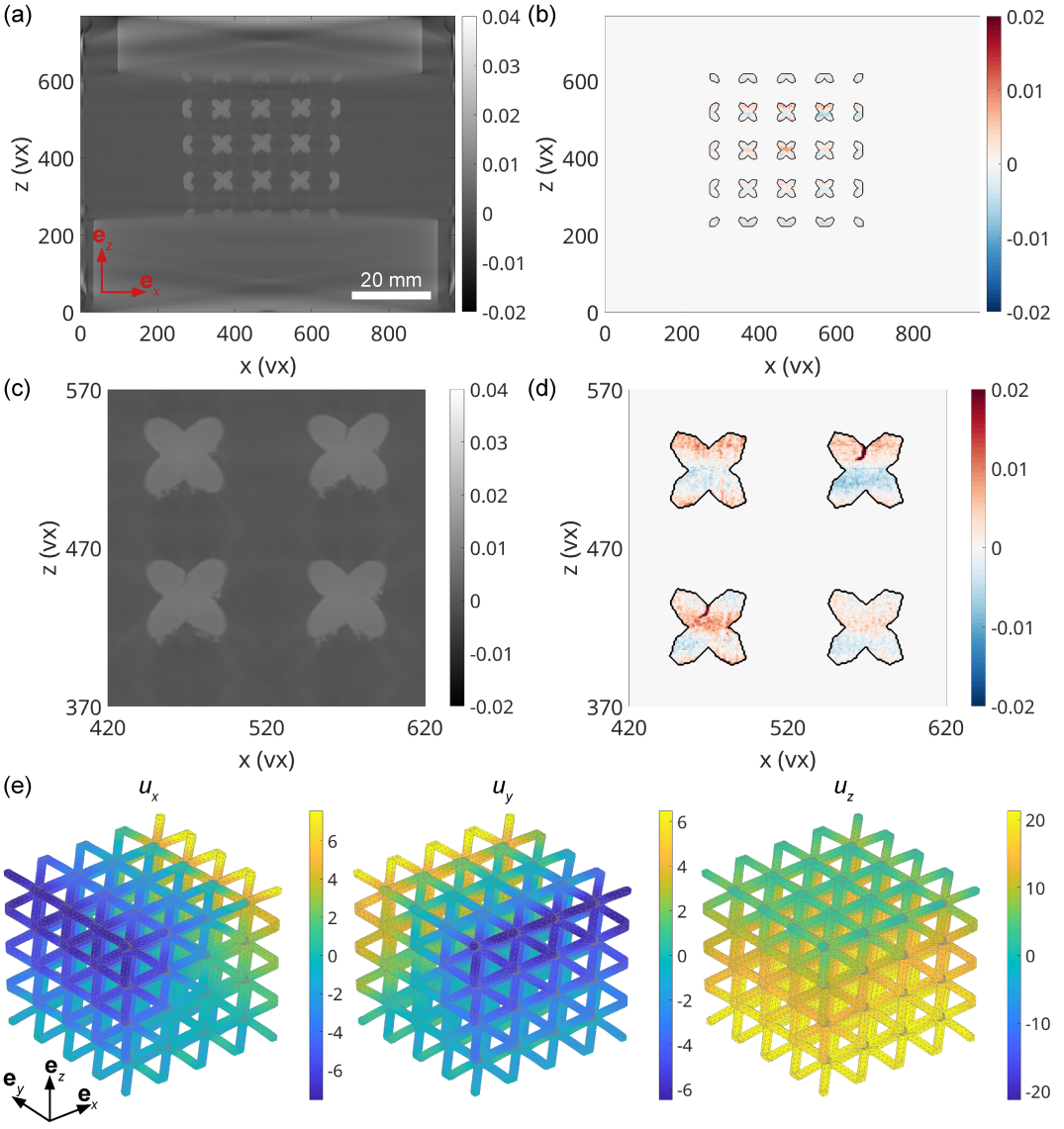

Figure 7. (a) Vertical slice at $T = 9$ (expressed in gray levels). (b) Corresponding dimensionless gray level residuals displayed in the reference configuration. (c)–(d) Zoomed-in views of sub-figures (a)–(b), respectively. (e) Measured displacement field components $\mathbf{u}_{\text{DVC}}(\mathbf{x}, T = 9)$, u_x, u_y, u_z expressed in vx.

each pixel of coordinate $\mathbf{r}$, for a rotation angle $\theta(t)$ (i.e. the tomograph turntable angle at time t). In the same way as DVC, the gray level residual is defined by

$$\rho_{\text{P-DVC}}(\mathbf{r}, t) = \Pi_{\theta(t)}\big[I_0\big(\cdot - \mathbf{u}(\cdot)\big)\big](\mathbf{r}) - p\big(\mathbf{r}, \theta(t)\big). \tag{6}$$

To measure 4D displacement fields $\mathbf{u}(\mathbf{x}, t)$, a spacetime separation is assumed

$$\mathbf{u}(\mathbf{x}, t) = \sum_{i}^{i_{\max}} \alpha_i(t)\mathbf{w}_i(\mathbf{x}), \tag{7}$$

with $\alpha_i(t)$ the temporal amplitude of mode i, whose spatial mode is $\mathbf{w}_i(\mathbf{x})$. Having $\mathbf{w}_i(\mathbf{x})$ modeled or derived from DVC measurements, only the temporal amplitudes $\alpha_i(t)$ are unknown

and identified in the P-DVC stage [13]. In this separation of variables, DVC is used to provide a high-fidelity yet temporally sparse spatial kinematic basis from a few tomographic scans, whereas P-DVC enriches the temporal sampling by estimating a small set of modal amplitudes for each treated projection. Consequently, the number of unknowns per time step is reduced from a full nodal displacement field to a few scalars, which significantly improves conditioning, lowers computational cost, and enables for interpolation of the kinematics between scans with sufficient sensitivity to capture, say, early nonlinearities [16].

In the same spirit as DVC, the temporal amplitudes are obtained from the minimization of the quadratic differences between the (re-)projected reference 3D image corrected by the displacement field and the acquired projection in the deformed state

$$\phi^2_{\text{P-DVC}}(\{\boldsymbol{\alpha}\}) = \sum_{\mathbf{r}} \Big(\Pi_{\theta(t)} \big[I_0\big(\cdot - \mathbf{u}(\cdot, \{\boldsymbol{\alpha}\})\big) \big] (\mathbf{r}) - p\big(\mathbf{r}, \theta(t)\big) \Big)^2 . \tag{8}$$

Further implementation details of projection enhanced DVC are found in Refs. [13,34,35]. Table 9 lists the main parameters of the P-DVC procedure.

2.4.1. *Projection processing*

After flat field corrections [23] and beam hardening correction (Figure 8(a)–(b)), the projections were masked (Figure 8(c)–(d)) in order to mitigate acquisition limitations in the vicinity of the compression platens where the X-ray absorption was too strong. It should be noted that the top and bottom platens were not meshed and therefore not projected yielding very high residuals in areas of the projection where they appear. The useful height of the projections then was 300 px, while the whole recorded width was used (i.e. 972 px, or ≈ 98 mm). It is worth noting that the chosen projection angle for load monitoring was $\theta(t) = 0$, $\forall\ t$.

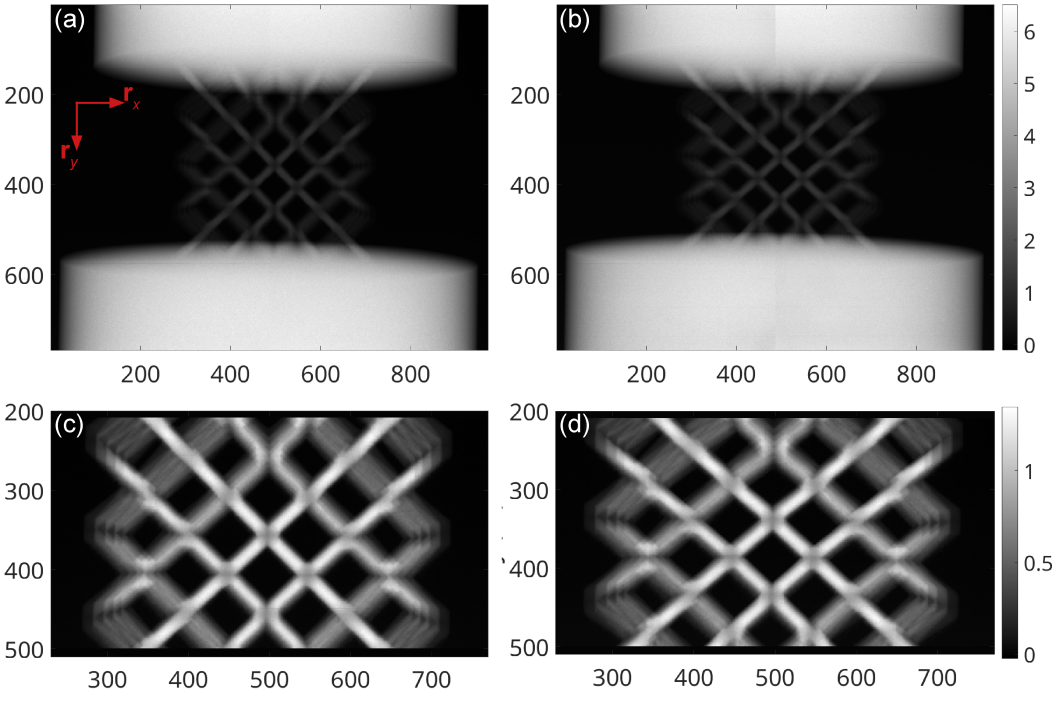

Figure 8. X-ray projections (expressed in gray levels). (a) At beginning of step 1, $p(\mathbf{r}, t = 0\,\text{h})$. (b) At end of dwell 9, $p(\mathbf{r}, t = 2.3\,\text{h})$. (c)–(d) Close-up view of the same masked projections.

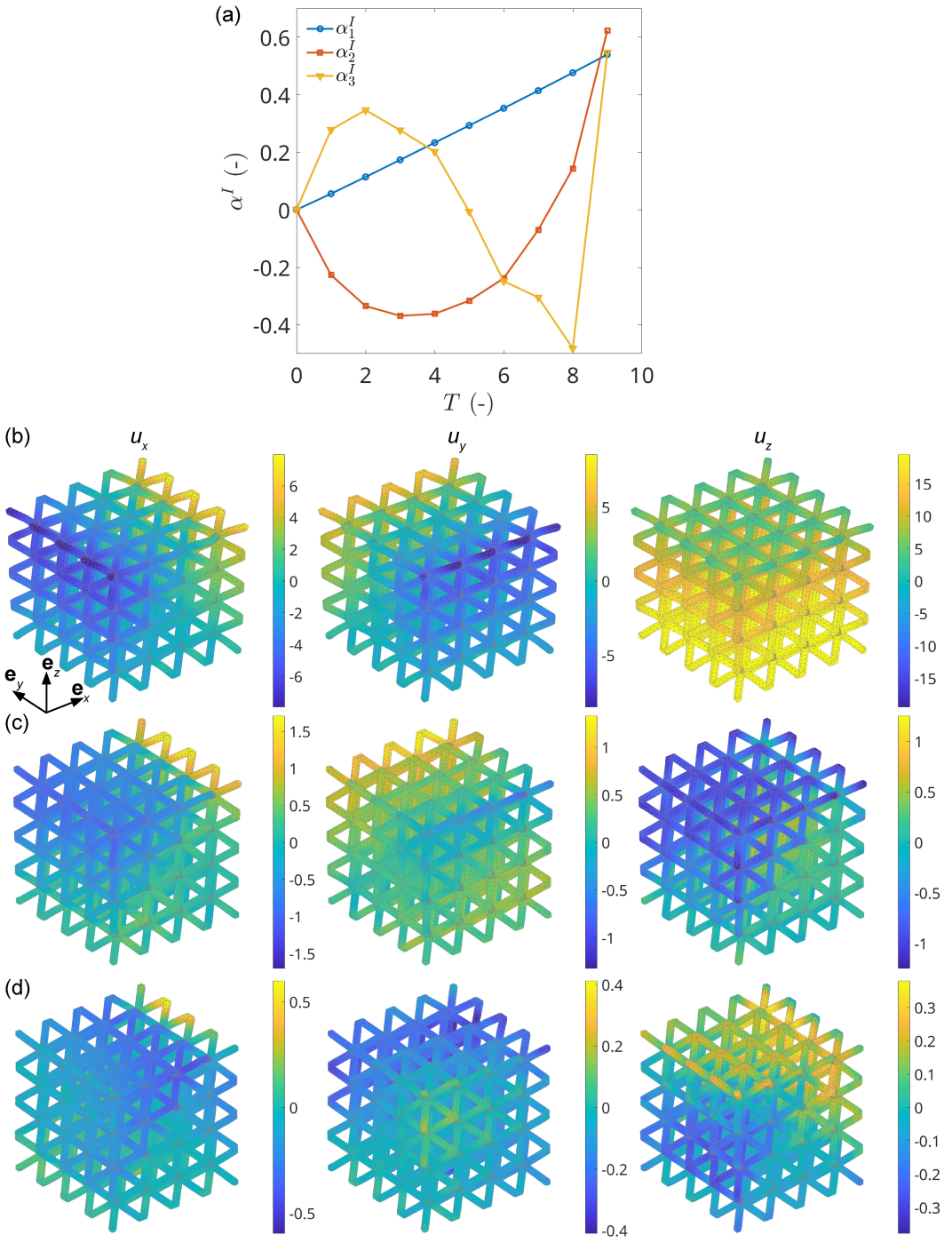

Figure 9. Basis I — (a) Amplitude α_i^{I} of the first three modes of the displacement fields obtained by SVD. Corresponding displacement fields $\alpha_m^{\mathrm{I}}(T)\mathbf{w}_m^{\mathrm{I}}(\mathbf{x})$ for $T = 9$: (b) mode $m = 1$ (def. factor: ×2); (c) mode $m = 2$ (def. factor: ×5); (d) mode $m = 3$ (def. factor: ×10).

2.4.2. *Reduced kinematic bases*

The second necessary element of the P-DVC protocol is to select the spatial modes (Equation (7)). In this study, three bases are proposed, namely, (I) data-driven model based on Singular Value Decomposition (SVD), (II) an elastic mechanical model, and (III) a data-enhanced mechanical model.

Basis I — Data-driven model. One way to construct the kinematics of the lattice sample deforming under compression is to perform an *a posteriori* SVD of the nine displacement fields measured by DVC

$$\mathbf{u}_{\mathrm{DVC}}(\mathbf{x},T)=\sum_{i=1}^{9}\alpha_i^{\mathrm{I}}(T)S_i^{\mathrm{I}}\mathbf{w}_i^{\mathrm{I}}(\mathbf{x}), \tag{9}$$

where the corresponding eigenvalues S_i^{I}, sorted in decreasing order, are listed in Table 1. The temporal and spatial components, respectively $\alpha_i^{\mathrm{I}}(T)$ and $\mathbf{w}_i^{\mathrm{I}}(\mathbf{x})$, constitute an orthonormal basis. Table 1 shows that the first eigenvalue S_1^{I} is at least one order of magnitude greater than those of the other modes. The associated displacement field $\alpha_1^{\mathrm{I}}(T=9)\mathbf{w}_1^{\mathrm{I}}(\mathbf{x})$ has a similar shape as a compression field in the z-direction (Figure 9(b)). The mode amplitude $\alpha_1^{\mathrm{I}}(T)$ increases linearly with T (Figure 9(a)). Mode 2, which is $S_2^{\mathrm{I}}\approx 2.6\times S_3^{\mathrm{I}}$, describes the shear band due to damage (emerging at $T=6$ with $\alpha_2^{\mathrm{I}}\approx -0.2$). Mode 3, becoming important when $T=8$, completes the damage field of mode 2 for the last stages of compression before failure of the lattice metamaterial. The last line of Table 1 reports the truncation error related to the DVC measurement uncertainty (Section 2.3.2)

$$\chi_u^2(M)=\left\|\{\mathbf{u}_{\mathrm{DVC}}\}-\{\mathbf{u}_M\}\right\|^2_{[\mathbf{Cov}_u]^{-1}}, \tag{10}$$

where $\{\mathbf{u}_{\mathrm{DVC}}\}$ gathers all measured nodal displacements, $\left\|\{\cdot\}^\top\right\|^2_{[\mathbf{Cov}_u]^{-1}}=\{\cdot\}[\mathbf{Cov}_u]^{-1}\{\cdot\}$, $[\mathbf{Cov}_u]$ is the covariance matrix associated with displacement measurements, here approximated by a diagonal matrix whose components are the variances of the displacement uncertainties associated with the selected regularization length (Figure 5), and $\{\mathbf{u}_M\}$ the corresponding nodal displacements of the decomposition truncated to M modes

$$\mathbf{u}_M^{\mathrm{I}}(\mathbf{x},T)=\sum_{m=1}^{M}\alpha_m^{\mathrm{I}}(T)S_m^{\mathrm{I}}\mathbf{w}_m^{\mathrm{I}}(\mathbf{x}). \tag{11}$$

The level of χ_u gives a good indication on the number of modes that correspond to signal instead of noise. Including only the first mode yields a non negligible error (i.e. 13 times the DVC uncertainty or 0.25 vx, which is already rather low). Including more modes decreases the truncation error. When $M=3$ modes are kept, the truncation error was less than 0.05 vx, which is only three times the standard displacement uncertainty of the DVC measurement. When $M\geq 4$, the associated truncation error χ_u is of the order of 1 or less, meaning that the residuals cannot be distinguished from the displacement uncertainties. Consequently, the maximum value of M was set to 3.

Table 1. Eigenvalues of SVD modes of the 9 DVC displacement fields, and corresponding (rounded) dimensionless truncation error.

	Number of modes, M								
	1	2	3	4	5	6	7	8	9
Eigenvalue, S_m^{I}	5165	216	82	37	20	9	6	4	4
χ_u	13	5	3	1	<1	<1	<1	<1	0

Figure 9(a) shows the history of the amplitudes $\alpha_m^{\mathrm{I}}(T)$ of the first three modes ($m \in \{1,2,3\}$) when $T \in [1,9]$. Figure 9(b)–(d) shows the corresponding displacement fields $\mathbf{u}_m^{\mathrm{I}}(\mathbf{x},T)$ for $T=9$.

Basis II — Elastic solution. The second kinematic basis proposes a linear elastic model of the compressed lattice. This basis should not be confused with mechanical regularization used in the previous DVC stage. The latter was introduced, as a local mechanical filter, only to stabilize the scan-wise DVC measurements, whereas basis II is a complete reduced kinematic description used in P-DVC analyses. The backtracked mesh was used (Figure 3) and static condensation [36] enables a purely elastic displacement field $\mathbf{w}_{\mathrm{elas}}(\mathbf{x})$ to be constructed when a unitary vertical displacement $u_z = 1\,\mathrm{vx}$ is applied on the bottom Dirichlet nodes of the mesh (i.e. the mobile part of the testing machine) $u_x = u_y = 0$ was also applied to these nodes to account for what was measured via DVC (this constraint is due to the presence of printing supports that were not included in the CAD model, which stiffened the structure for the first row of beams), and a prescribed vertical displacement $u_z = 0$ on the top Dirichlet nodes with unconstrained u_x and u_y displacements, with the material Poisson's ratio $\nu = 0.36$. This purely elastic field is completed with 3 additional rigid-body translations (RBT), leading to a basis with 4 elements

$$\left\{\mathbf{w}_{\mathrm{elas}}(\mathbf{x}),\ \mathbf{e}_x,\ \mathbf{e}_y,\ \mathbf{e}_z\right\}, \tag{12}$$

where $\mathbf{e}_i$ denote unitary vectors along direction $i \in \{x,y,z\}$. The (up to) four temporal amplitudes are obtained by solving the least squares minimization

$$\left\{\boldsymbol{\alpha}^{\mathrm{II}}(T)\right\} = \arg\min_{\{\boldsymbol{\beta}\}\in\mathbb{R}} \left\| \mathbf{u}_{\mathrm{DVC}}(\mathbf{x},T) - \sum_{i=1}^{i_{\max}} \beta_i^{\mathrm{II}}\,\mathbf{w}_i^{\mathrm{II}}(\mathbf{x}) \right\|_2^2. \tag{13}$$

The displacement field is then reconstructed as

$$\mathbf{u}_{\mathrm{elas}}(\mathbf{x},T) = \sum_{i=1}^{i_{\max}} \alpha_i^{\mathrm{II}}(T)\,\mathbf{w}_i^{\mathrm{II}}(\mathbf{x}). \tag{14}$$

The amplitudes obtained with the elastic basis are reported in Table 2, together with the associated truncation errors $\chi_u(i_{\max})$ and their incremental decrease $\Delta\chi_u(i_{\max})$ when successive modes are added. The first mode, corresponding to the elastic compression amplitude $\alpha_{\mathrm{elas}}^{\mathrm{II}}$, carries most of the information: with only this mode, the truncation error remains large ($\chi_u = 86.9$) but already captures the dominant compressive kinematics of the lattice. Introducing the vertical translation t_z significantly reduces the error ($\Delta\chi_u = -54$), showing that part of the discrepancy with DVC is related to global rigid-body motion along the compression axis. In contrast, adding the horizontal translations t_x and t_y has only a marginal effect, with $\Delta\chi_u = -4$ and -3, respectively. These modes are in the order of magnitude of the measurement noise and therefore do not contribute meaningfully to the description of the deformation. As a result, the purely elastic compression mode enriched with the vertical translation is retained in the following, while the transverse translations are disregarded. The dominant correction comes from t_z, which likely captures the combined compliance of the testing machine and the imperfect enforcement of boundary conditions at the platens, whereas transverse translations remain at the measurement noise level.

As shown in Figure 10, the truncation error systematically increases with the deformation level for all bases, reflecting the growing drift from a purely elastic kinematics. The error growth is steeper when only the elastic mode is kept (i.e. $i_{\max} = 1$), whereas the addition of the vertical translation t_z ($i_{\max} = 2$) significantly attenuates this trend. Beyond this first correction, the curves corresponding to t_x and then t_y ($i_{\max} = 3,4$) remain very close to that when $i_{\max} = 2$, confirming their negligible influence throughout the entire loading history.

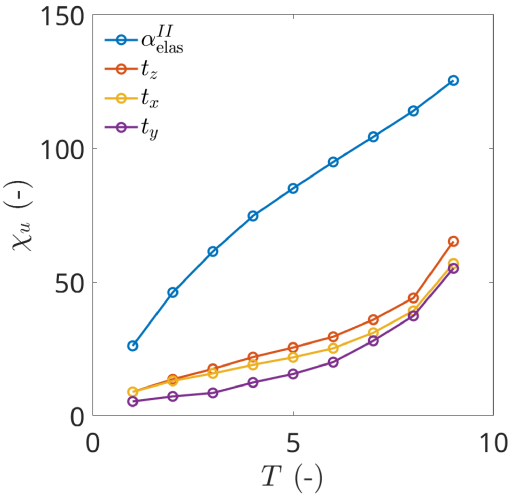

Figure 10. Evolution of the truncation error for basis II for all DVC fields when $i_{\max} = 1, 2, 3$ and 4.

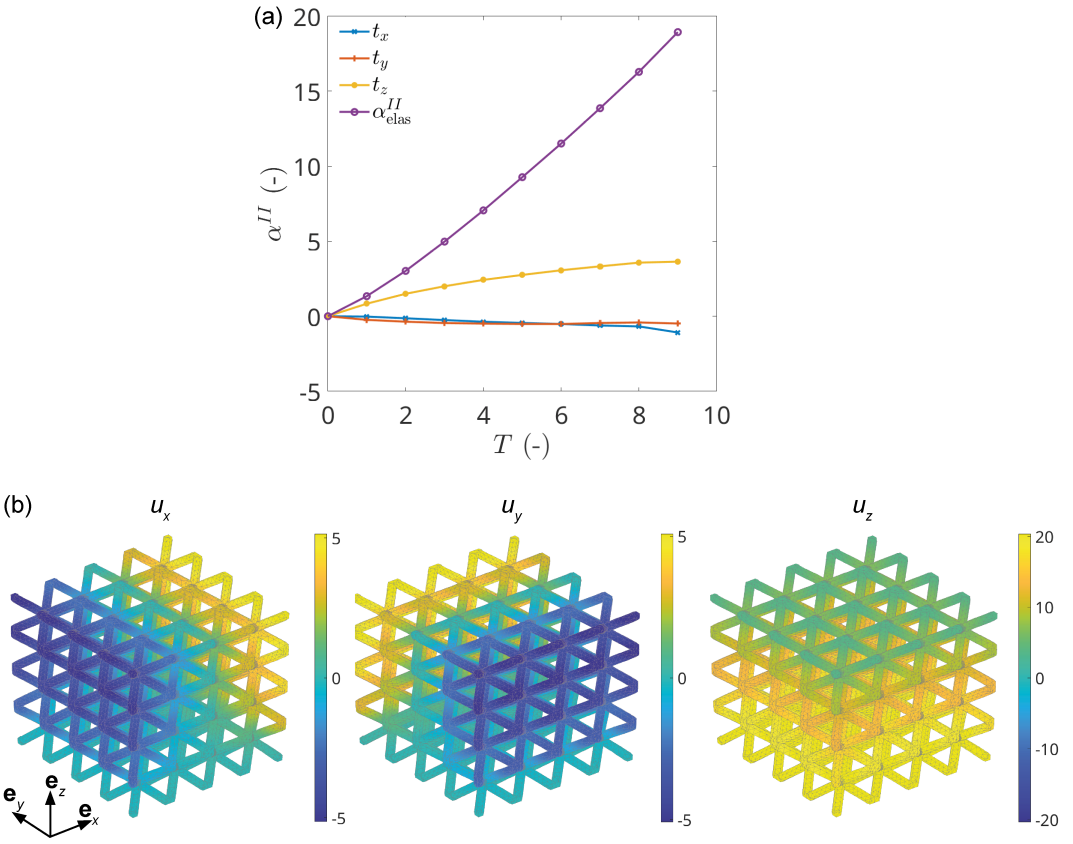

Figure 11. Model II basis — (a) Amplitudes t_x, t_y, t_z, and $\alpha^{\text{II}}_{\text{elas}}$. (b) Elastic displacement field $\alpha^{\text{II}}_{\text{elas}}(T)\mathbf{w}_{\text{elas}}(\mathbf{x})$ for $T = 9$ (u_x, u_y, u_z components expressed in vx, def. factor: ×2).

The resulting field for turn $T = 9$ is shown in Figure 11(b). The amplitude associated with compression (here denoted $\alpha^{\mathrm{II}}_{\mathrm{elas}}$) reaches ≈ 19 vx. The translation in the z-direction monotonically increases up to $t_z(T = 9) \approx 3.6$ vx and $t_x \approx t_y \approx 0 \ \forall \ T$ meaning that no translation occurred in the transverse directions. It is therefore reasonable to attribute t_z to the compliance of the experimental setup.

Table 2. Dimensionless truncation error as a function of the considered number of modes $i_{\max}$ and corresponding variation for the elastic basis.

Mode number, i	1	2	3	4
Mode amplitude α^{II}_i	$\alpha^{\mathrm{II}}_{\mathrm{elas}}$	t_z	t_x	t_y
Number of mode, $i_{\max}$	1	2	3	4
$\chi_u(i_{\max})$	87	33	29	26
$\Delta\chi_u(i_{\max})$	—	−54	−4	−3

Basis III — Data-enhanced mechanical model. This basis also uses the elastic model of basis II as well as results of DVC analyses. When the elastic part of the displacement fields is subtracted from the measured DVC displacement fields

$$\mathbf{u}_{\mathrm{comp}}(\mathbf{x}, T) = \mathbf{u}_{\mathrm{DVC}}(\mathbf{x}, T) - \mathbf{u}_{\mathrm{elas}}(\mathbf{x}, T), \tag{15}$$

the complementary part of the displacement field $\mathbf{u}_{\mathrm{comp}}(\mathbf{x}, T)$ is obtained. Here again, SVD was computed on these complementary displacement fields using the 9 scans, and then truncated

$$\mathbf{u}_{\mathrm{comp}}(\mathbf{x}, T) = \sum_{k=1}^{K} \alpha^{\mathrm{III}}_k(T) S^{\mathrm{III}}_k \mathbf{w}^{\mathrm{III}}_k(\mathbf{x}), \tag{16}$$

where $\mathbf{w}^{\mathrm{III}}_k(\mathbf{x})$ are the spatial modes, $\alpha^{\mathrm{III}}_k(T)$ the corresponding temporal modes, and the eigenvalues S^{III}_k are gathered in Table 3. The spatial and temporal components are orthonormal and sorted by decreasing order. It is worth noting that the eigenvalue of the first mode is approximately 14 times smaller than that obtained from the SVD of the original DVC displacement fields (Table 1), meaning that the elastic description is capturing the first-order kinematics. In the following, $K = 2$ modes were kept to capture the complementary displacement field with an error of 4× the DVC displacement uncertainty.

Table 3. Eigenvalues of the SVD modes for the complementary (non-elastic) part of the 9 DVC displacement fields, and corresponding (rounded) dimensionless truncation error.

	Number of mode, K								
	1	2	3	4	5	6	7	8	9
Eigenvalue, S^{III}_k	564	159	62	36	18	7	5	5	4
χ_u	10	4	2	1	<1	<1	<1	<1	0

Figure 12(a) shows the history of the amplitudes $\alpha^{\mathrm{III}}_k(T)$ ($k \in \{1,2\}$) and Figure 12(b)–(c) displays the displacement fields $\alpha^{\mathrm{III}}_k(T) S^{\mathrm{III}}_k \mathbf{w}^{\mathrm{III}}_k(\mathbf{x})$ of the first two modes of these complementary contributions when $T = 9$. Mode $k = 1$, which is more than 4× greater than mode $k = 2$, exhibits a rather smooth nonlinear increase with compression and compensates mode 1 until $T = 8$. It reaches its maximum amplitude ($\alpha^{\mathrm{III}}_2 \approx 0.6$) when $T = 9$.

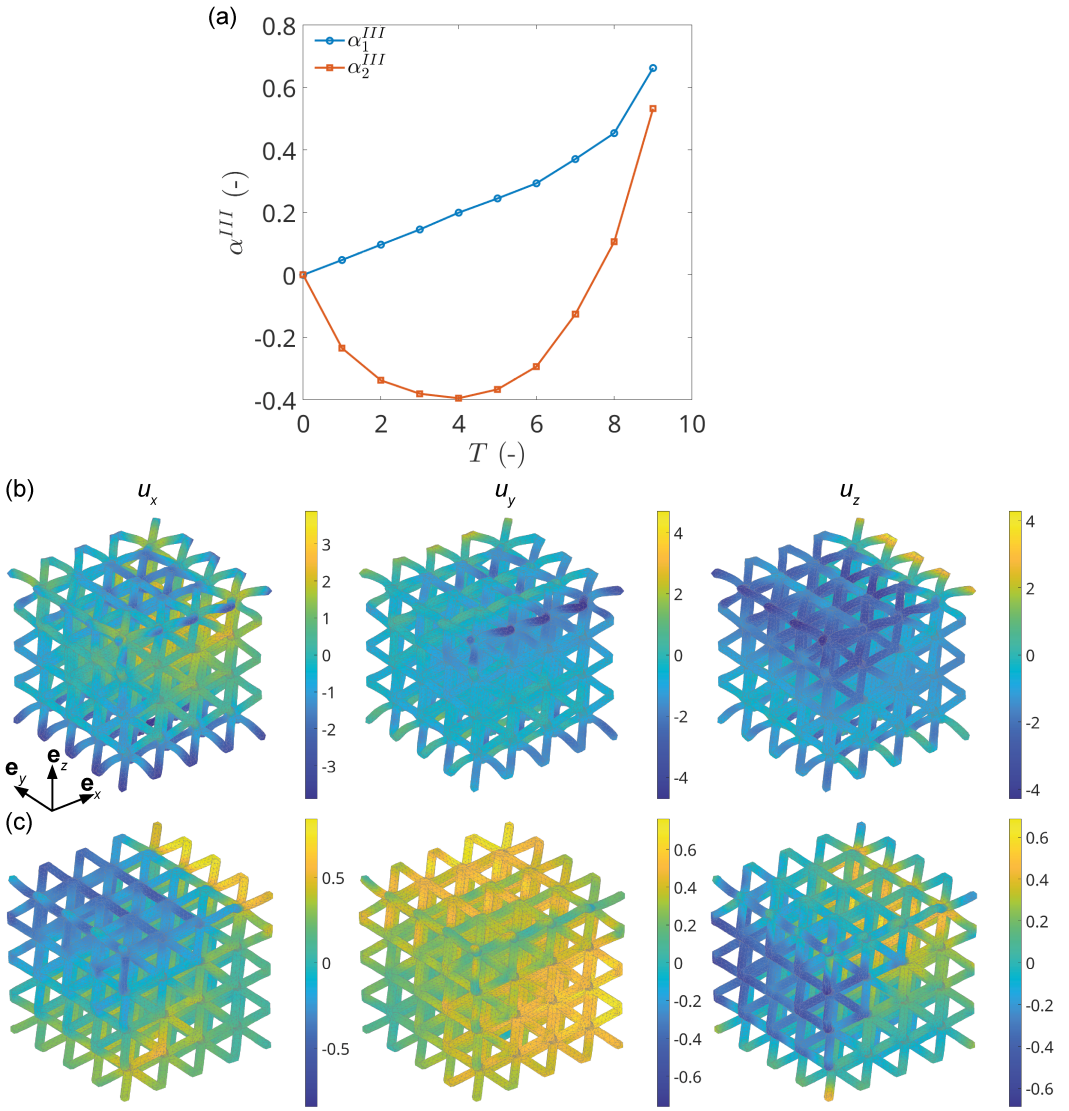

Figure 12. Model III basis — (a) Amplitude $\alpha_k^{\mathrm{III}}(T)$ of the first two modes of the complementary part of the DVC displacement fields. Corresponding displacement fields $\alpha_k^{\mathrm{III}}(T)S_k^{\mathrm{III}}\mathbf{w}_k^{\mathrm{III}}(\mathbf{x})$ for $T = 9$ (u_x, u_y, u_z components expressed in vx): (b) mode $k = 1$ (def. factor: ×5); (c) mode $k = 2$ (def. factor: ×10).

Summary of reduced kinematic models. Three reduced kinematic bases were considered (Table 4):

Basis I: relies on a data-driven SVD basis extracted from the DVC fields and truncated to the first few modes to maximize accuracy at minimum modal dimension.

Basis II: uses a mechanics-only basis composed of a purely elastic compressive mode and rigid-body translations to favor interpretability.

Basis III: is hybrid in the sense that the elastic fields (similar to basis II space) are complemented with SVD modes of the complementary residual, thereby capturing early nonlinearities while retaining a physically interpretable framework.

In all cases, the temporal amplitudes are identified via P-DVC by minimizing the projected residuals for each treated projection.

Table 4. Summary of the three reduced kinematic bases used in the P-DVC analyses.

Basis	Spatial basis	Amplitudes	Displacement field
I (Data-driven)	First SVD modes of DVC fields $\mathbf{w}^{\mathrm{I}}_m(\mathbf{x})$. Basis truncated to first M modes (here $M = 1-3$).	$\alpha^{\mathrm{I}}_m(t)$, $m = 1,\dots,M$	$\mathbf{u}(\mathbf{x},t) = \sum_{m=1}^{M} \alpha^{\mathrm{I}}_m(t)\, S^{\mathrm{I}}_m\, \mathbf{w}^{\mathrm{I}}_m(\mathbf{x})$
II (Elastic)	Elastic compression mode $\mathbf{w}_{\mathrm{elas}}(\mathbf{x})$ + rigid-body translation(s)	$\alpha^{\mathrm{II}}_{\mathrm{elas}}(t)$, $t^{\mathrm{II}}_z(t)$ (opt. $t^{\mathrm{II}}_x(t)$, $t^{\mathrm{II}}_y(t)$)	$\mathbf{u}(\mathbf{x},t) = \alpha^{\mathrm{II}}_{\mathrm{elas}}(t)\,\mathbf{w}_{\mathrm{elas}}(\mathbf{x}) + t^{\mathrm{II}}_z(t)\,\mathbf{e}_z$
III (Hybrid)	Elastic fields enriched with SVD modes $\mathbf{w}^{\mathrm{III}}_k(\mathbf{x})$ of the complementary DVC part; truncated to K modes (here $K = 1-2$).	$\alpha^{\mathrm{III}}_{\mathrm{elas}}(t)$, $t^{\mathrm{III}}_z(t)$, $\alpha^{\mathrm{III}}_k(t)$, $k = 1,\dots,K$	$\mathbf{u}(\mathbf{x},t) = \alpha^{\mathrm{III}}_{\mathrm{elas}}(t)\,\mathbf{w}_{\mathrm{elas}}(\mathbf{x}) + t^{\mathrm{III}}_z(t)\,\mathbf{e}_z + \sum_{k=1}^{K} \alpha^{\mathrm{III}}_k(t)\, S^{\mathrm{III}}_k\, \mathbf{w}^{\mathrm{III}}_k(\mathbf{x})$

2.4.3. *Uncertainty quantification*

The uncertainty of the P-DVC procedure was assessed from the measurement of the temporal amplitudes $\{\boldsymbol{\alpha}\}$ in the reduced bases in the unloaded state before the first step (i.e. a total of $\mathcal{N} = 50$ projections were analysed) and was assessed on the corresponding 3D nodal displacements $\{\mathbf{u}\}$ whose temporal fluctuations (i.e. standard deviations) were computed. Their RMS level then corresponds to the standard displacement uncertainty $\mathrm{std}(u_{\text{P-DVC}})$. Figure 13 leads the following comments:

- the bases with the lowest number of modes yielded the lowest uncertainty levels;
- the order of magnitude of the highest uncertainties in P-DVC (i.e. basis I with $M = 3$ and basis III) are one order of magnitude below the DVC displacement uncertainties (because the amplitudes are associated with highly sensitive displacement modes).

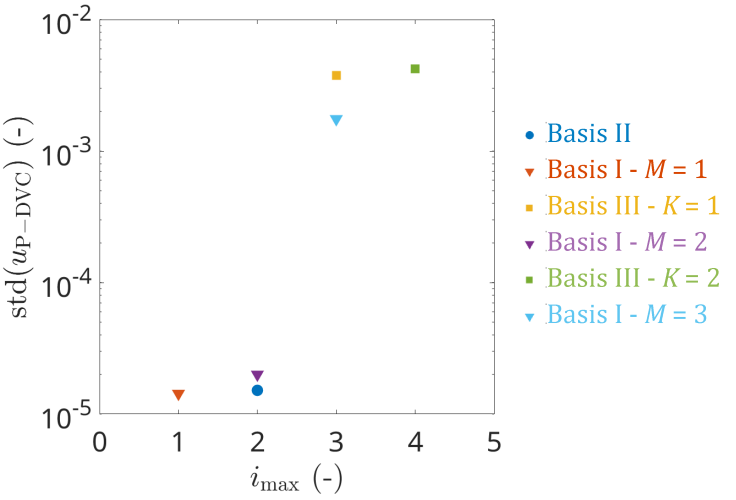

Figure 13. P-DVC standard displacement uncertainty $\mathrm{std}(\{\boldsymbol{u}_{\text{P-DVC}}\})$ vs. number of modes $i_{\max}$ for the three bases.

2.4.4. *P-DVC calculations*

As the P-DVC procedure operates in the projection space, special care must be taken when defining the volume support used for the projection. In the present case, the printed material exhibited low internal contrast, so that the useful information in the radiographs was mainly governed by the edges. Unlike scan-wise DVC, which registers one 3D volume with another one, P-DVC requires that the whole volume intensity be included in the numerical projection. A mesh fitted too tightly to the reconstructed geometry may locally be positioned slightly inside the actual material because of backtracking imperfections, surface roughness, printing defects, or slight reconstruction blur. The corresponding outer part of the specimen would not be projected, leading to projection errors. For this reason, a slightly enlarged mesh was used to ensure that the full projected material of the specimen contributed to the comparison with the experimental radiographs. The enlarged mesh was only considered for the projection calculations in P-DVC analyses. The identified displacements were then transferred back to the nominal, tighter mesh by interpolation, and all reconstructed displacement fields were finally expressed on the nominal mesh for comparison with DVC and FE results.

This mesh was created as the first one from a CAD model with beams 3 mm in diameter instead of 2 mm (the other dimensions were unaltered). Using the same meshing procedure as for the DVC mesh, it resulted in $\mathcal{N}_{\text{node}} = 43\,707$ and $\mathcal{N}_{\text{elem}} = 167\,487$ with an average element length of ≈ 5 vx. The aforementioned displacement modes $\mathbf{w}_i$ were interpolated to their nearest neighbor onto the wider mesh for the P-DVC calculations. The amplitudes of the modes that were found with the procedure were used to reconstruct the solutions on the normal mesh for comparison purposes with DVC. For P-DVC runs, the convergence criterion was defined on the modal amplitudes only (Table 9). A unique threshold was selected to allow for convergence even when the modes were not very sensitive, and such that the amplitude fluctuations remained negligible with respect to the measured levels.

The computational time to solve Equation (8) is proportional to the number of deformation modes $i_{\max}$ characterized by their displacement fields $\mathbf{w}_i$. Here, $1 \leq i \leq 3$ considering $M = 1, \ldots, 3$ modes in Equation (11), $i_{\max} = 2$ for basis II in Equation (14), $i_{\max} = 3$ for basis III with $K = 1$, and $i_{\max} = 4$ for basis III when $K = 2$ in Equation (16). In the procedure, the main computational cost is due to the deformation of the 3D reference image and the Eulerian/Lagrangian coordinate switch.

Considering the testing machine crosshead displacement speed (i.e. $\dot{U} = 5\,\mu$m/s), the projection acquisition rate (i.e. 2.7 fps), and the resolution (i.e. 100.8 µm per vx), one in ten projections (i.e. $\mathcal{N} = 936$ out of a total of $\mathcal{N} = 9362$) were used for the computation of the modal amplitudes $\{\boldsymbol{\alpha}(t)\}$. Note that this corresponds, in the present setting, to a temporal resolution of 3.7 s, whereas a resolution of 0.37 s could in principle be achieved if all projections were processed. It took about 35 h (i.e. ≈ 2 min per projection), for one basis component ($i_{\max} = 1$), and up to 72 h (i.e. ≈ 5 min per projection) for four modes ($i_{\max} = 4$), on a 12 core Xeon W-2265 CPU with 128 GB RAM and RTX A5000 GPU with 24 GB VRAM server. At the current computational cost, the proposed framework should therefore be regarded as an offline proof of concept.

3. Results

In Figures 14 and 15 are plotted the history of the modal amplitudes measured by P-DVC normalized by the expected amplitude for $T = 9$, $\alpha^\star(t) = \alpha_{\text{P-DVC}}(t)/\alpha_{\text{DVC}}(T = 9)$, where $\alpha_{\text{DVC}}(T = 9)$ is given by the SVD (11). The amplitudes of the DVC modes are plotted at the center of the scan acquisition time lapse and normalized in the same way (i.e. $\alpha^\star(T) = \alpha_{\text{DVC}}(T)/\alpha_{\text{DVC}}(T = 9)$).

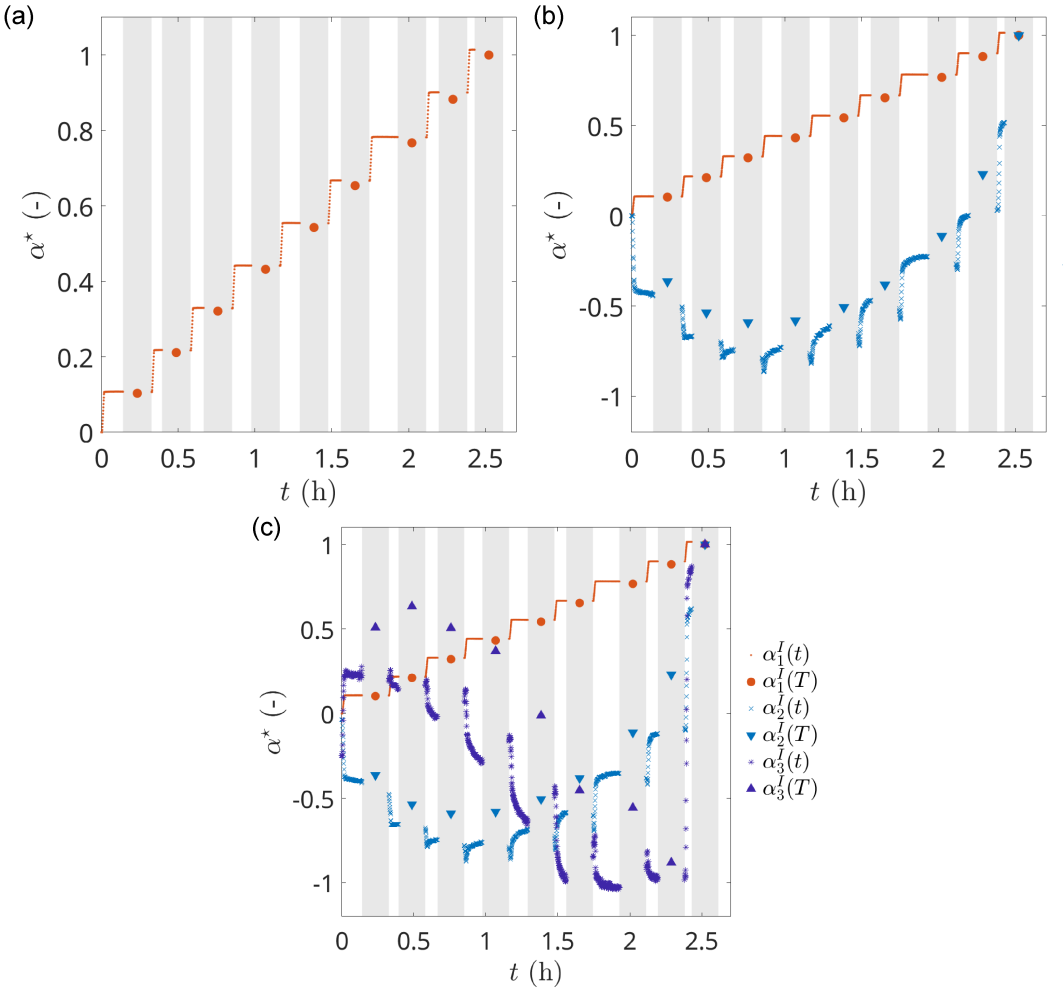

Figure 14. Basis I — Normalized amplitudes $\alpha^\star$: (a) $M = 1$; (b) $M = 2$; (c) $M = 3$.

For the SVD-based kinematics (basis I):

- When $M = 1$ (Figure 14(a)), P-DVC slightly overestimates α_1^{I} by ~2 % relative to the DVC results.
- With $M = 2$ (Figure 14(b)), α_1^{I} remains close to the DVC levels, while α_2^{I} is underestimated during loading but approaches the DVC level by the end of step 9. Notably, $|\alpha_2^{\mathrm{I}}|$ increases during loading and decreases during dwell.
- When $M = 3$ (Figure 14(c)), α_1^{I} remains accurate; α_2^{I} is slightly underestimated until late steps where it becomes overestimated; α_3^{I} follows the DVC results closely. The sudden variation of α_3^{I} at step 9 is attributed to the inception of damage during loading and is well captured by P-DVC.

For the elastic/hybrid descriptions (bases II–III):

- Basis II (Figure 15(a)): the t_z amplitude is overestimated by up to ~30 % for step 9; the purely elastic amplitude $\alpha_{\mathrm{elas}}^{\mathrm{II}}$ is slightly overestimated overall but matches the DVC levels at the end of step 9. Both grow linearly during loading; small changes during dwell likely

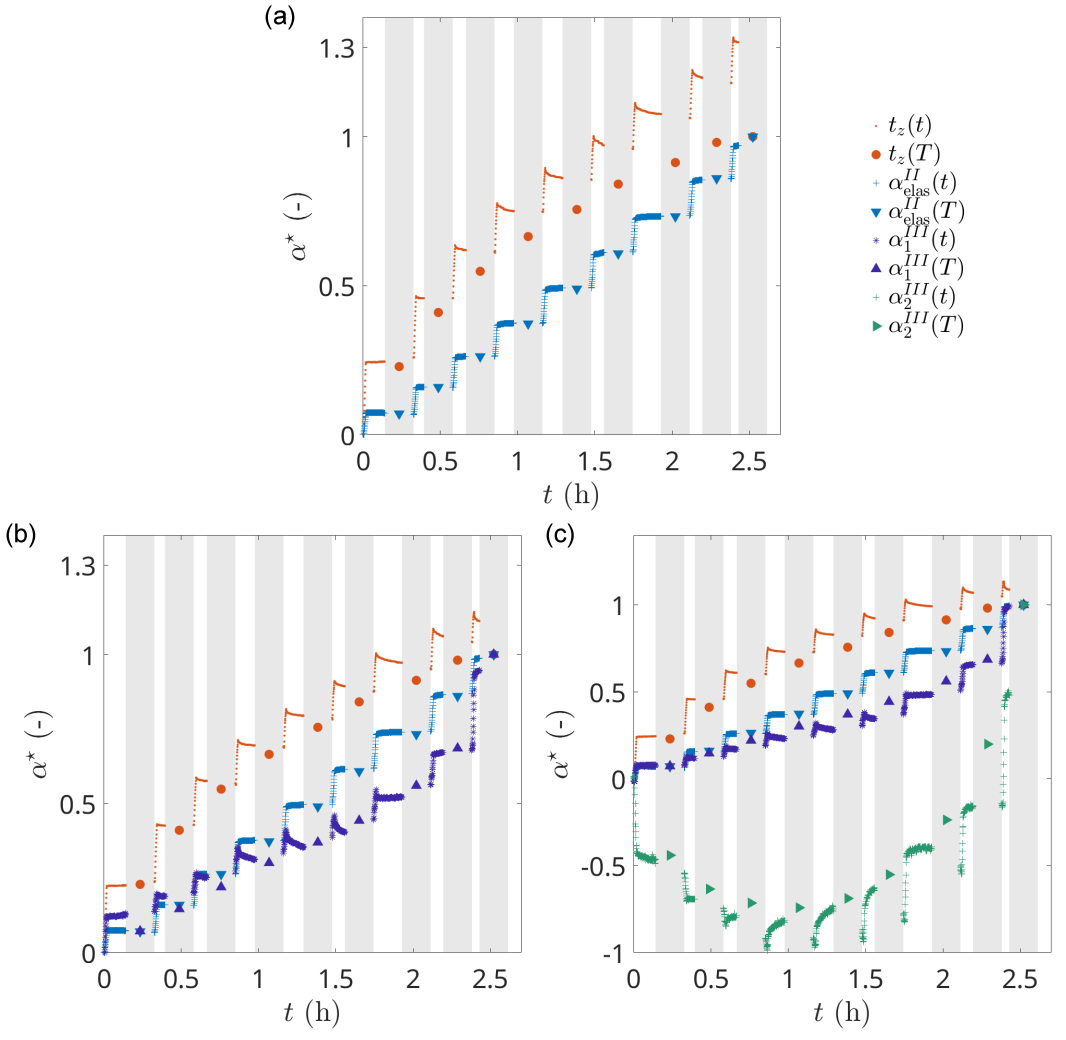

Figure 15. Normalized amplitudes: (a) basis II; (b) basis III, $K = 1$; (c) basis III, $K = 2$ complementary modes.

compensate the RBT decrease. This apparent compensation arose because the dominant compression mode and the rigid-body translation t_z both contributed to the vertical displacement component u_z. During dwell, a slight decrease of the force may therefore be offset by a small increase in t_z.

- Basis III with $K = 1$ complementary mode (Figure 15(b)): t_z better matches the DVC levels, $\alpha^{\text{III}}_{\text{elas}}$ is slightly affected, and the first complementary amplitude α^{III}_1 is poorly estimated at early steps but converges by steps 4–5.
- Basis III with $K = 2$ complementary modes (Figure 15(c)): including α^{III}_2 does not improve t_z, nor $\alpha^{\text{III}}_{\text{elas}}$, nor α^{III}_1. The second complementary amplitude α^{III}_2 follows rather well the DVC results and exhibits a strong nonlinear evolution with t during dwell.

Figure 16 shows the dimensionless pixel-wise residuals of the last projection of dwell 9 $\rho^\star(\mathbf{x}, t = 2.3\text{h})$ for the 6 kinematic bases studied herein. All 6 propositions led to $\left|\rho^\star(\mathbf{x}, t = 2.3\text{h})\right| \leq 0.1$ in the most deformed state highlighting that they all are relevant in the description

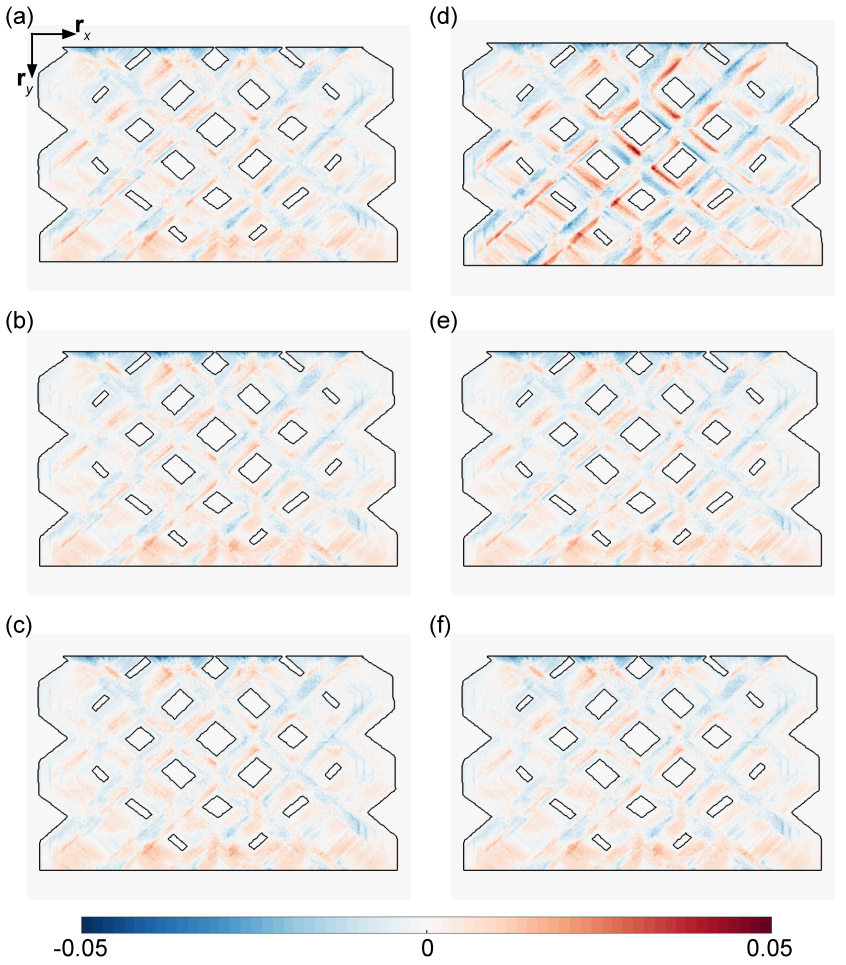

Figure 16. Dimensionless residuals $\rho^\star(\mathbf{r}, t = 2.3\,\text{h})$. Basis I with (a) $M = 1$, (b) $M = 2$, (c) $M = 3$ modes. (d) Basis II. Basis III with (e) $K = 1$ and (f) $K = 2$ complementary modes.

of the compression experiment. The elastic model (basis II) exhibits higher localized residuals; enriching it with complementary modes (basis III) and/or using SVD modes (basis I) reduces the residuals and their spatial extent.

Figure 17 shows that the dimensionless Root Mean Square (RMS) residual $\rho^\star = \rho(\mathbf{r}, t)/\Delta p(t)$ of the P-DVC analyses is less than 3.6 % of the projection dynamic range $\Delta p(t) = \max\big(p(\mathbf{r}, t)\big) - \min\big(p(\mathbf{r}, t)\big)$ (including air and the sample), for the entire duration of the experiment for any chosen kinematic basis. On closer inspection, the simplest model (i.e. basis II, purely elastic compression + t_z) has the highest residuals while basis I with $M = 3$ modes achieves the lowest residuals. In between, the basis III enriched with $K = 2$ complementary modes led to decreased residuals.

Another way to quantify the trustworthiness of the P-DVC measurements is to evaluate the norm of the nodal displacement differences compared to the DVC results

$$\Delta(\mathbf{x}, T, t) = \left\| \mathbf{u}_{\text{DVC}}(\mathbf{x}, T) - \mathbf{u}_{\text{P-DVC}}(\mathbf{x}, t \neq T) \right\|, \tag{17}$$

and the mean nodal displacement difference $\big\langle \Delta(T, t) \big\rangle$. It should be noted that $T \neq t$, the

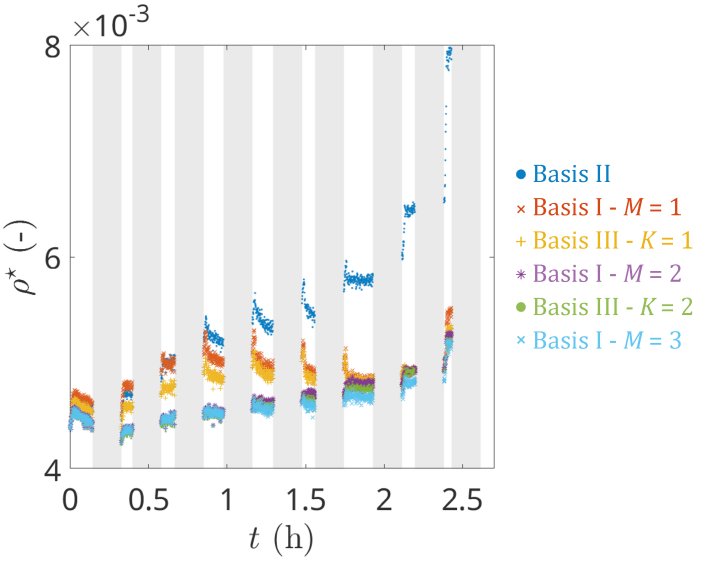

Figure 17. RMS dimensionless residual $\rho^\star$ vs. time for the six investigated bases.

comparison of P-DVC displacement fields is calculated only for times t close to T namely (i) the last dwell projection before scan acquisition, and (ii) the first projection before loading.

Figure 18 shows the change of $\langle \Delta(t) \rangle$ evaluated on the two projections that encompass the DVC displacement field measured at turn T. The insets display the norm of the displacement differences for the last projection of dwell 9 $\Delta(\mathbf{x}, t = 2.3\,\text{h})$. As expected, the simplest model (i.e. basis II) exhibits the highest differences, which increase monotonically with the compression level to reach $\langle \Delta \rangle \approx 2\,\text{vx}$ when $T = 9$ with a standard deviation of 1 vx. The inset of Figure 18(d) shows that the shear band on the top left of the sample, which was not described by the elastic model, led to the highest nodal difference together with the bottom and top layers of the lattice. Conversely, basis I fields were such that $\langle \Delta(t) \rangle < 1\,\text{vx}$ for any number of modes $M \in \{1,2,3\}$ and the compression state $T \in [1,9]$ (Figure 18(a)–(c)). When the basis I is enriched (i.e. with two and three modes), $\langle \Delta \rangle < 0.5\,\text{vx}$ (Figure 18(b) and (c)). Similarly, when the elastic model is enriched by $K = 1$ or $K = 2$ complementary modes, the mean nodal displacement difference decreases by a factor ≈ 2 (Figure 18(d)–(f)). For all models, the two projections used to evaluate the differences Δ did not produce the same results, thereby indicating that the sample had moved during scan acquisitions (Figure 2(c)).

4. Discussion

The present study demonstrated that the temporal resolution of displacement fields could be increased by more than two orders of magnitude compared to classical DVC analyses, thanks to the use of P-DVC combined with reduced kinematic bases. Two complementary strategies were explored. First, a data-driven decomposition of the DVC displacement fields using singular value decomposition (SVD) allowed for the reconstruction of intermediate states, with three modes being sufficient to reproduce the DVC fields down to sub-voxel differences. Second, an elastic model provided a first-order approximation of the measured kinematics with minimal computational cost. These two approaches, when combined, form the basis of the hybrid model that

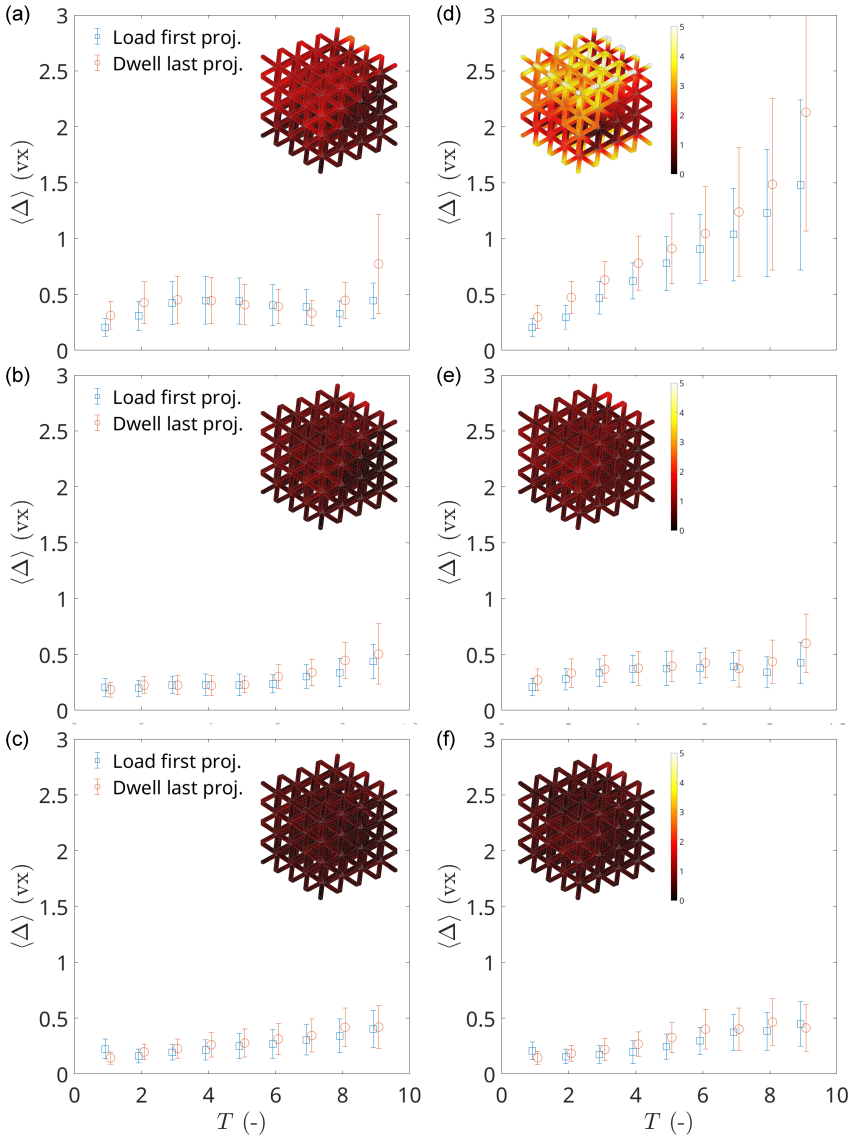

Figure 18. Mean nodal displacement difference $\langle\Delta\rangle$, the error bars correspond to the standard deviation of the nodal displacement difference, the insets display $\Delta(\mathbf{x}, t = 2.3\,\mathrm{h})$ of the last projection of dwell 9. Basis I with (a) $M = 1$, (b) $M = 2$, (c) $M = 3$ modes. (d) Basis II. Basis III using (e) $K = 1$ and (f) $K = 2$ complementary modes. The two projection markers are moved horizontally around the turn number for better readability.

captures both the main elastic trend and the leading nonlinear contributions. Such modal enrichment strategies align with recent reduced-order developments that couple mechanics-based fields with data-driven corrections to combine interpretability and predictive accuracy [4,14].

The scaling of modal amplitudes with the prescribed displacement provided further insight into the deformation mechanisms. The dominant amplitude (α_1^{I} in the SVD basis and $\alpha_{\mathrm{elas}}^{\mathrm{II}}$ in the elastic basis) grew approximately linearly with the crosshead displacement, reflecting the global compressive response of the lattice. By contrast, the second SVD amplitude and the first complementary mode of the hybrid basis scaled quadratically with U, consistent with

the emergence of nonlinear effects such as shear banding, local buckling, or friction at the interfaces. Importantly, the complementary modes remained an order of magnitude smaller than the dominant elastic modes, highlighting that the nonlinear contributions were captured as subtle corrections to the main kinematics. In particular, the complementary modes not only reduced the truncation errors but also provided a clear signature of nonlinear mechanisms, which were difficult to anticipate with a purely elastic field.

The analysis of truncation errors clarified the balance between representativity and interpretability. With the elastic basis, including the vertical rigid-body translation t_z removed most of the mismatch with DVC, whereas horizontal translations (t_x, t_y) contributed only at the uncertainty level. In the data-driven basis, three SVD modes sufficed to reduce the truncation error at the DVC uncertainty level. This result suggests that a minimal hybrid basis (purely elastic compression and t_z, and one or two complementary modes) offers the best compromise between compactness, interpretability, and predictive accuracy.

The experiment enabled for the *a posteriori* analysis of deformation modes at a rate of 0.27 Hz (i.e. one state every 3.7 s), compared to the 11 min of scan acquisitions, the temporal resolution was multiplied by ≈ 100. Although the present study used one in ten radiographs, the results confirm that temporally dense monitoring is achievable. Future work should investigate efficiency improvements (e.g. via coarser binning, GPU acceleration, or reduced-domain projections) to bring computation times closer to real-time operations.

The location of damage in the diagonal layer of beams in the lattice at 45° in the (x, z) plane makes it difficult to monitor it for the selected projection angle (i.e. $\theta = 0°$). A sensitivity study for the second deformation mode with respect to the projection angle shows that its amplitude could have been more easily captured when $\theta = 90°$, whereas the first mode was not very sensitive to θ. This choice would have improved the estimates of the amplitudes $\alpha_2^{\mathrm{I}}(t)$ and $\alpha_1^{\mathrm{III}}(t)$ with possibly even lower projection residuals. In practice, choosing a small set of discrete angles (optimized for their sensitivity) or using dual-source systems [37] would improve identifiability of non-axial modes without a prohibitive overhead.

The RMS projection residuals (Figure 17) show several variations at different times (i.e. at the hour scale, between load acquisitions and in a fainter way during load acquisitions). Taking a closer look, in particular for the first steps (from 1 to 7), the residual increased during load and before stabilizing in the dwell steps. The jumps between the scans may be due to X-ray source variations and/or minute boundary condition changes during CT scan acquisitions.

Two limitations should be noted. First, gray-level conservation and the omission of the platens in the forward model concentrate residuals near the contact surfaces (Figure 16). Explicitly meshing the platens or further masking those regions may reduce bias in amplitude estimations. Second, because contrast within struts was weak at the chosen resolution, the method primarily utilized the printed interface gradients. At higher resolutions or with added contrast (e.g. markers, phase contrast), the sensitivity to internal, fine, strains would increase, potentially enabling finer kinematic descriptions to be captured. Addressing these limitations will be essential for transferring the methodology to a larger spectrum of architected and natural materials, particularly when fine-scale mechanisms govern their global behavior.

5. Conclusion

A spacetime experimental-numerical framework combining FE-based Digital Volume Correlation (DVC) and projection-based DVC (P-DVC) has been proposed and applied to *in situ* compression of an additively manufactured lattice structure made of aluminum alloy. Three reduced-order strategies have been considered, namely, a purely data-driven decomposition, a

mechanics-based (elastic) model, and a hybrid mechanics-data approach. The following main outcomes have been established.

First, a temporal resolution corresponding to the time between two treated radiographs has been achieved, outperforming by orders of magnitudes classical DVC analyses based on tomographic volumes. This gain has enabled for quasi-continuous tracking of the deformation process throughout the entire loading sequence. In the present study, only one in ten projections were processed, which corresponded to a temporal resolution of 3.7 s. (In principle, a finer resolution down to 0.37 s could have been reached had all radiographs been exploited; yet this choice would come at the expense of a substantially higher computational cost.) This observation underlines the need for more efficient implementations to fully benefit from the temporal richness of the projection data.

Second, a systematic comparison of three reduced-order strategies showed that the hybrid (purely elastic + RBT enriched with a few SVD modes of the complementary field) delivered the best trade-off between interpretability and representativity. It preserved the clear physical meaning of the elastic amplitudes and the machine-induced longitudinal translation, while the added data-driven modes selectively captured early nonlinearities that the elastic model alone could not reproduce. In practice, the hybrid basis achieved projection residuals comparable to the purely data-driven SVD approach, with mean nodal displacement differences close to those of truncated SVD modes. At the same time, it avoided the loss of physical interpretability inherent to a purely data-driven basis, and remained computationally frugal compared to higher-dimensional SVD truncations. A practical kinematic enrichment guideline emerges, namely, start from a purely elastic + t_z baseline, and incrementally add one complementary mode only when the truncation error or the amplitude histories reveal emerging nonlinear behavior.

The series of projections acquired after the final 3D scan acquisition could be analyzed specifically, which would provide further information beyond standard scan-wise DVC [16] in a regime where nonlinear variations may become large. The projections acquired during the tomographic scans may also be processed within the same P-DVC framework. In the present work, the analysis was deliberately restricted to the fixed-angle loading/dwell radiographs in order to isolate and assess the effect of the reduced kinematic bases in a simpler configuration.

Overall, the projection enhanced DVC framework has provided temporally dense and spatially resolved measurements of additively manufactured lattices. By bridging data-driven and mechanics-based descriptions, the methodology enhanced both the interpretability and the reliability of *in situ* measurements. The approach is expected to be applicable to a broad range of architected materials and to contribute to improved understanding of deformation and failure processes in such complex structures. Future work will aim at extending this framework to other material classes, incorporating more advanced constitutive models, and constructing reduced bases from mechanically simulated fields to capture richer nonlinear behaviors, especially from scan 4 onward, when the measured response departed from the simplified elastic assumption. Exploiting double X-ray sources [37] would also offer a promising route to further increase the spatial and temporal resolutions.

Declaration of interests

The authors do not work for, advise, own shares in, or receive funds from any organization that could benefit from this article, and have declared no affiliations other than their research organizations.

Appendix A. Printing parameters and material composition

This appendix presents the information related to the printing process and the material used to manufacture the lattice specimen. Table 5 collects information about the equipment that was used to produce the specimen and the printing parameters. Table 6 gives the detailed material composition of the AlSi10Mg powder used to produce the studied metamaterial.

Table 5. Printing hardware and parameters.

Equipment	
EOS M290 LPBF (EOS GmbH)	
Layer thickness	30 µm
Substrate temperature	35 °C
Laser	IPG laser GmbH ytterbium-fiber laser
Wavelength	1060–1100 nm
Laser power	370 W
Laser beam diameter	80 µm
Laser velocity	1300 mm/s
Hatch spacing	130 µm

Table 6. Material composition.

Al%	**Si%**	**Mg%**	**Fe%**	**Ti%**	**Cr%**	**Ni%**	**Cu%**	**Mn%**
Bulk	10.22	0.306	0.253	0.15	0.034	0.032	0.007	0.004

Appendix B. X-ray tomography hardware and image analysis parameters

This appendix gathers the information about the acquisition process and the DVC analysis parameters. Table 7 collects the information about the hardware acquisition parameters, namely, the X-ray source and detector settings during the acquisition of the scans as well as the voxel size of the reconstructed volumes. The radiograph acquisitions were performed with a 2×2 hardware binning. A further numerical 2×2 binning was then applied to all projections prior to reconstruction and P-DVC analyses, which explains the final effective 4×4 binning reported for the reconstructed volumes and loading projections. Tables 8 and 9 list the main parameters of the FE-DVC procedure as well as those of P-DVC.

Table 7. X-ray tomograph parameters.

Hardware	
Tomograph	North Star Imaging X50+
X-ray source	XRayWorX XWT-240-CT
Target / Anode	W (reflection mode)
Filter	none
Voltage	160 kV
Current	200 µA
Focal spot size	5 µm
Source to detector	510 mm
Source to object	160 mm
Voxel size	50.4 µm
Detector	Dexela 2923
Definition	1944×1536 pixels (2×2 binning)
CT scan parameters	
Number of projections	1000
Angular amplitude	360°
Frame average	10 per projection
Exposure time	1/15 s
Acquisition duration	11 min 06 s
Reconstruction algorithm	FDK+SIRT [22] (2×2 binning)
Gray Levels amplitude	16 bits
Volume size	$972 \times 972 \times 768$ voxels (4×4 binning)
Voxel size after binning	100.8 µm
Field of view	$98.0 \times 98.0 \times 77.4\,\text{mm}^3$
Loading projection parameters	
Angular amplitude	0°
Frame average	1 per projection
Exposure time	1/15 s
Effective frame rate	2.7 fps
Definition	972×768 pixels (4×4 binning)

Table 8. DVC analysis parameters.

DVC software	
Correli 3.2 [27]	
Image filtering	none
Element length (mean)	4.6 vx (or 0.46 mm)
Shape functions	linear (T4 elements [25])
Mesh	see Figure 3
Number of nodes	30 155
Number of elements	97 893
Matching criterion	penalized sum of squared volume differences
Regularization length	$\ell_m = 125$ vx (or 12.6 mm)
Image interpolant	cubic
Displacement noise floor	see Figure 5
Convergence criterion	$\left\|\{\delta \boldsymbol{v}\}\right\| < 10^{-2}$ vx

Table 9. P-DVC analysis parameters.

P-DVC software	
Correli 3.2 [27]	
Image filtering	none
Matching criterion	sum of squared projection differences
Spatial kinematic regularization	see Table 4
Temporal kinematic regularization	none
Image interpolant	cubic
Convergence criterion	$\left\|\{\delta \boldsymbol{\alpha}\}\right\| < 10^{-2}$

References

[1] E. Maire and P. J. Withers, "Quantitative X-ray tomography", *Int. Mater. Rev.* **59** (2014), no. 1, pp. 1–43.

[2] B. K. Bay, T. S. Smith, D. P. Fyhrie and M. Saad, "Digital volume correlation: three-dimensional strain mapping using X-ray tomography", *Exp. Mech.* **39** (1999), no. 3, pp. 217–226.

[3] B. K. Bay, "Methods and applications of digital volume correlation", *J. Strain Anal. Eng. Des.* **43** (2008), pp. 745–760.

[4] A. Buljac, C. Jailin, A. Mendoza, et al., "Digital volume correlation: review of progress and challenges", *Exp. Mech.* **58** (2018), no. 5, pp. 661–708.

[5] J.-Y. Buffiere, E. Maire, J. Adrien, J. P. Masse and E. Boller, "In situ experiments with X ray tomography: an attractive tool for experimental mechanics", *Exp. Mech.* **50** (2010), no. 3, pp. 289–305.

[6] L. Mazy and G. Kerckhofs, "A review of in-situ mechanical testing combined with X-ray microfocus computed tomography: application and current challenges for biological tissues", *Tomogr. Mater. Struct* **8** (2025), article no. 100062 (12 pages).

[7] A. C. Kak and M. Slaney, *Principles of computerized tomographic imaging*, Classics in Applied Mathematics, Society for Industrial and Applied Mathematics, 2001.

[8] E. Maire, C. Le Bourlot, J. Adrien, A. Mortensen and R. Mokso, "20 Hz X-ray tomography during an in situ tensile test", *Int. J. Fract.* **200** (2016), no. 1, pp. 3–12.

[9] E. Maire, A. Owen, J.-Y. Buffiere and P. J. Withers, "A synchrotron X-ray study of a Ti/SiCf composite during in situ straining", *Acta Mater.* **49** (2001), no. 1, pp. 153–163.

[10] F. García-Moreno, P. H. Kamm, T. R. Neu, et al., "Tomoscopy: Time-resolved tomography for dynamic processes in materials", *Adv. Mater.* **33** (2021), no. 45, article no. 2104659 (13 pages).

[11] E. Zwanenburg, M. Williams and J. M. Warnett, "Review of high-speed imaging with lab-based x-ray computed tomography", *Meas. Sci. Technol.* **33** (2021), no. 1, article no. 012003 (18 pages).

[12] C. Jailin, A. Buljac, A. Bouterf, F. Hild and S. Roux, "Fast 4D tensile test monitored via X-CT: Single projection based Digital Volume Correlation dedicated to slender samples", *J. Strain Anal. Eng. Des.* **53** (2018), no. 7, pp. 473–484.

[13] V. Kosin, A. Fau, C. Jailin, B. Smaniotto, T. Wick and F. Hild, "A projection-based approach to extend digital volume correlation for 4D spacetime measurements", *Comptes Rendus. Mécanique* **351** (2023), no. G2, pp. 265–280.

[14] A. Mandić, V. Kosin, C. Jailin, Z. Tomičević, B. Smaniotto and F. Hild, "Damage detection in a polymer matrix composite from 4D displacement field measurements", *Materials* **16** (2023), no. 18, article no. 6300 (28 pages).

[15] A. Vrgoč, V. Kosin, B. Smaniotto, C. Jailin, Z. Tomičević and F. Hild, "4D full-field measurements over the entire loading history: Evaluation of different temporal interpolations", *Coupled Syst. Mech.* **12** (2023), no. 6, pp. 503–517.

[16] V. Kosin, B. Smaniotto, M. Tarantino, A. Fau, T. Wick and F. Hild, "Quantifying damage in an AlSi10Mg porous metamaterial through projection-enhanced DVC", *Meas. Sci. Technol.* **36** (2025), no. 7, article no. 075002 (23 pages).

[17] A. Mandic, V. Kosin, B. Smaniotto, L. Salvi, M. G. Tarantino and F. Hild, "Damage quantification in an AlSi10Mg cellular metamaterial using 4D measurements", *Meas. Sci. Technol.* **36** (2025), no. 8, article no. 085017 (16 pages).

[18] K. Bertoldi, V. Vitelli, J. Christensen and M. Van Hecke, "Flexible mechanical metamaterials", *Nat. Rev. Mater.* **2** (2017), no. 11, pp. 1–11.

[19] X. Zheng, W. Smith, J. Jackson, et al., "Multiscale metallic metamaterials", *Nat. Mater.* **15** (2016), no. 10, pp. 1100–1106.

[20] T. DebRoy, H. L. Wei, J. S. Zuback, et al., "Additive manufacturing of metallic components — Process, structure and properties", *Prog. Mater. Sci.* **92** (2018), pp. 112–224.

[21] J. Y. Buffière, E. Maire, J. Adrien, J. P. Masse and E. Boller, "In Situ Experiments with X ray Tomography: an Attractive Tool for Experimental Mechanics", *Exp. Mech.* **50** (2010), no. 3, pp. 289–305.

[22] W. Van Aarle, W. J. Palenstijn, J. Cant, et al., "Fast and flexible X-ray tomography using the ASTRA toolbox", *Opt. Express* **24** (2016), no. 22, pp. 25129–25147.

[23] J. Lifton and T. Liu, "Ring artefact reduction via multi-point piecewise linear flat field correction for X-ray computed tomography", *Opt. Express* **27** (2019), no. 3, pp. 3217–3228.

[24] T. Taillandier-Thomas, S. Roux, T. F. Morgeneyer and F. Hild, "Localized strain field measurement on laminography data with mechanical regularization", *Nucl. Instrum. Methods Phys. Res., Sect. B* **324** (2014), pp. 70–79.

[25] F. Hild, A. Bouterf, L. Chamoin, et al., "Toward 4D mechanical correlation", *Adv. Model. Simul. Eng. Sci.* **3** (2016), no. 1, article no. 17 (26 pages).

[26] P. Auger, T. Lavigne, B. Smaniotto, M. Spagnuolo, F. Dell'Isola and F. Hild, "Poynting Effects in Pantographic Metamaterial Captured via Multiscale DVC", *J. Strain Anal. Eng. Des.* **56** (2021), no. 7, pp. 462–477.

[27] H. Leclerc, J. Neggers, F. Mathieu, F. Hild and S. Roux, *Correli 3.0*, Agence pour la Protection des Programmes, Paris (France), IDDN.FR.001.520008.000.S.P.2015.000.31500, 2015.

[28] F. dell'Isola, P. Seppecher, M. Spagnuolo, et al., "Advances in Pantographic Structures: Design, Manufacturing, Models, Experiments and Image Analyses", *Contin. Mech. Thermodyn.* **31** (2019), no. 4, pp. 1231–1282.

[29] H. Leclerc, J.-N. Périé, F. Hild and S. Roux, "Digital volume correlation: what are the limits to the spatial resolution?", *Mech. Ind.* **13** (2012), no. 6, pp. 361–371.

[30] R. Vargas, V. Kosin, J. Lachambre, J. Adrien, C. Jailin, S. Roux and E. Maire, "Image-based geometry calibration for a double-tomograph", *Meas. Sci. Technol.* **37** (2026), no. 1, article no. 015404 (18 pages).

[31] P. C. Hansen, "The L-Curve and its use in the numerical treatment of inverse problems", in *Computational inverse problems in electrocardiography* (P. Johnston, ed.), Advances in Computational Bioengineering, vol. 5, WIT Press, 2000, pp. 119–142.

[32] C. Jailin, A. Buljac, A. Bouterf, M. Poncelet, F. Hild and S. Roux, "Self-calibration for lab-μCT using space-time regularized projection-based DVC and model reduction", *Meas. Sci. Technol.* **29** (2018), no. 2, article no. 024003 (13 pages).

[33] C. Fragnaud, C. Remacha, J. Betancur and S. Roux, "CAD-based X-ray CT calibration and error compensation", *Meas. Sci. Technol.* **33** (2022), no. 6, article no. 065024 (14 pages).

[34] T. Taillandier-Thomas, S. Roux and F. Hild, "Soft route to 4D tomography", *Phys. Rev. Lett.* **117** (2016), no. 2, article no. 025501 (5 pages).

[35] C. Jailin, A. Bouterf, M. Poncelet and S. Roux, "In situ μ CT-scan mechanical tests: fast 4D mechanical identification", *Exp. Mech.* **57** (2017), no. 8, pp. 1327–1340.

[36] R. J. Guyan, "Reduction of stiffness and mass matrices", *AIAA J.* **3** (1965), no. 2, p. 380.

[37] E. Maire, G. Bonnard, J. Adrien, X. Boulnat, J. M. Létang and J. Lachambre, "Dual beam microfocus high-energy tomography: Towards multimodal and faster laboratory experiments", *Tomogr. Mater. Struct* **5** (2024), article no. 100030 (10 pages).